Supplementary material for.

Fine Particle Liquid Water and Acidity over North American Cities during the Summer of 2023

Table of Contents

S1: Other Instrumentation.

The following describes other instrumentation also used in the analysis of the AEROMMA data.

PM_1 ion concentrations were measured using a Particle-into-Liquid Sampler (PILS) (Orsini et al., 2003) coupled to a Bretchel fraction collector system (Sorooshian et al., 2006). Particles were sampled through the NASA Langley Aerosol Research Group inlet (LARGE; McNaughton et al., 2007), which was shared across all aerosol instruments on the DC-8 except the AMS (which used a separate inlet). From the LARGE sampling line, particles were subsampled into the PILS through a pressure-controlled inlet (PCI). When the ambient pressure dropped below 450 mb, the PCI automatically switched to sampling cabin air. A non-rotating MOUDI impactor stage provided a PM_1 size cut (50% transmission at 1 μm aerodynamic diameter at 1 atm; Marple et al., 1991). Two annular denuders coated with sodium carbonate and phosphorous acid were used to remove inorganic acidic and basic gases in order to limit possible positive artifacts from dissolving in the PILS collection liquid. Liquid samples were collected in vials every 2 minutes (1.2 mL per vial) and analyzed offline by ion chromatography. A Dionex ICS-3000 ion chromatograph was used to measure water-soluble potassium. An eluent generator provided a concentration of 20 mM methanesulfonic acid at a flowrate of 0.5 mL/min to perform the separation on a Dionex IonPac CS12A analytical column (3 x150 mm). The injection volume was 190 μL with a complete run time of 17 min. The PILS uncertainty is 10%. More details can be found in Sullivan et al. [2019,2022].

Particle number size distributions were measured aboard the DC-8 using an Ultra-High Sensitivity Aerosol Spectrometer (UHSAS; Droplet Measurement Technologies). The UHSAS sizes individual particles via light scattering from a 1054 nm intracavity laser, providing size-resolved number concentrations at 1 Hz over the dry diameter range 0.063–1.0 μm (Kupc et al., 2018). Sizing was calibrated with ammonium sulfate aerosol, with reported uncertainties of +23%/-51% in derived particle volume due to refractive index variability. UHSAS-derived volume concentrations were used to evaluate AMS + SP2 PM_1 mass via the density comparison described in Sect. 3.1.

Acetonitrile (CH_3CN) concentrations were measured at 1 Hz using a H_3O^+ Proton-Transfer Reaction Time-of-Flight Mass Spectrometer (VOCUS-PTR-MS) through a Teflon inlet at a flow

rate of 0.1–2 L min^{-1}, with a reported uncertainty of ~30% and a detection limit of 0.009 ppbv (Gkatzelis et al., 2024). Refractory black carbon (rBC) mass concentration was measured at 1 Hz by a single-particle soot photometer (SP2) over the size range of 90-550nm and scaled up to correct for average accumulation-mode rBC mass outside of detection range (Schwarz et al., 2006). rBC was used alongside AMS mass concentrations to calculate total PM_1.

NO_x (NO + NO_2) was measured by the NOAA Laser-Induced Fluorescence (LIF) instrument (Rollins et al., 2020), in which NO is excited at 215 nm and fluorescence is detected between 255 and 267 nm; NO_2 is photolyzed to NO at 295 nm prior to detection. Calibration uncertainties were ±6% for NO and ±9% for NO_2, with boundary layer precisions of ~2 ppt and ~10 ppt, respectively. O_3 was measured by the NOAA fast-response NO-induced chemiluminescence (CL) instrument, in which ambient O_3 reacts with excess NO reagent in a controlled-pressure reaction vessel and the resulting chemiluminescence is detected by photomultiplier tubes (Chace et al., 2025; Bourgeois et al., 2020). Calibration was performed in-flight via standard additions of onboard-generated O_3, yielding an accuracy of ±5% and 1 Hz precision of 50 ppt.

S2: Spatial Distributions of Aerosol Composition, ALWC, and pH Within Individual Study Regions

S2.1. Overview

The main text focuses on the East–West and inter-city patterns in PM_1 aerosol liquid water content (ALWC) and pH that support the paper's central argument: that aerosol pH is low, and near-invariant across diverse North American urban environments in summer, governed primarily by the TSO_4–TNO_3–TNH_x–H_2O thermodynamic system, with TNO_3 having a minor role in most locations. Within each region, the airborne measurements also show spatial variability in aerosol and gas-phase composition driven by local source distributions, meteorology, and urban–rural gradients. These localized distributions are consistent with the inter-city findings presented in the main text and are provided as supplementary material to maintain focus on the broader regional analysis.

Spatial distributions of key gas-phase and aerosol species are shown in Figs. S7–S11, organized by region and smoke condition. Predicted ALWC and pH are overlaid on the spatial maps for selected flights to illustrate whether local compositional variability translated into meaningful local-scale variability in these thermodynamic quantities. We find that, consistent with the main text, pH remained constrained within approximately 1 unit even at the within-city scale, while ALWC tracked local RH and inorganic loading as expected. These observations are discussed region by region below.

S2.2. Spatial Variability Under Low/No-Smoke Conditions

S2.2.1. New York City (Fig. S7)

During the August 16 low/no-smoke flight over the New York metropolitan area, aerosol and gas-phase concentrations were elevated over the urban core, with the most pronounced enhancements observed over Manhattan, consistent with the concentration of vehicular and stationary sources in that area.

ALWC was substantially elevated over Manhattan relative to the surrounding metropolitan area, driven by the combination of higher PM_1 inorganic loading and the high ambient RH on this flight (mean 83%). Despite this spatial variability in ALWC, predicted pH remained constrained near 1.5–2.3 across the entire flight domain, with no systematic relationship between local ALWC enhancements and pH. This spatially uniform pH within the various cities is similar to the inter-city result described in the main text: the NH_3/NH_4^+ and HNO_3/NO_3^- buffering mechanism suppresses pH variability even where ALWC varies substantially at the local scale.

S2.2.2. Chicago (Fig. S8)

During the August 12 low/no-smoke flight over the Chicago metropolitan area, PM_1 species concentrations were relatively spatially uniform across metropolitan corridor sampled by the

aircraft. Total PM_1 (5.31 ± 1.49 μg m^{-3} for this flight) was lower than in NYC or LA (campaign mean: 11.98 ± 8.16 μg m^{-3}), consistent with the lower emission densities implied by lower NO_x and O_3 concentrations (Table S1).

A notable feature was slightly elevated TNH_x (predominantly NH_3) in the western portion of the metropolitan area, consistent with proximity to agricultural sources in western Illinois and southern Wisconsin. This pattern is relevant to the inter-city comparison: it illustrates that urban NH_3 measurements can be influenced by upwind agricultural emissions.

Over Lake Michigan, PM_1 mass concentrations and ALWC were elevated relative to inland areas. This enhancement was associated with higher ambient RH over the lake surface and, in some cases, slightly lower temperatures, which together promote hygroscopic growth and aqueous-phase uptake. Predicted pH over the lake was similar to that observed over the urban core despite the higher ALWC, again illustrating the buffering effect of the system. Slightly elevated pH values of 2.5–3.0 were observed over the northwestern suburbs of Chicago, collocating with areas of higher ambient NH_3, consistent with the pH-elevating effect of elevated TNH_x described in Sect. 4.1 of the main text. These values were still well within the 1.5–2.5 range that characterizes the broader campaign.

S2.2.3. Los Angeles (Fig. S9)

The three low/no-smoke flights over the Los Angeles metropolitan area (August 23, 25, and 26) revealed clear spatial structure in aerosol and gas-phase composition, reflecting the diverse source landscape of the LA basin. PM_1 concentrations were generally higher over land than over the near-shore and port areas, consistent with the dominance of mobile, ship and possibly industrial sources in the inland basin. Both NH_3 and HNO_3 were elevated within the metropolitan area and along the Interstate 10 and 210 corridors through the Anaheim–Burbank–Riverside transect, pointing to vehicular emissions as the dominant proximate source. This is consistent with the high TNH_x (6.20 ± 2.12 μg m^{-3}) and TNO_3 (10.39 ± 4.61 μg m^{-3}) observed over LA relative to the eastern cities.

Sulfate showed a distinctive spatial pattern, with systematically elevated concentrations over Long Beach and the San Pedro Bay area, likely reflecting contributions from ship exhaust in the heavily trafficked port region. OA concentrations were consistently enhanced over forested areas north of the LA basin, suggesting a significant secondary OA contribution from regional volatile organic compound oxidation. These spatial features in composition did not produce corresponding spatial structure in pH: predicted pH across the LA basin was consistently near 2.0–2.5, and the higher sulfate near Long Beach did not elevate local acidity (lower pH) relative to the rest of the domain. This is consistent with the thermodynamic arguments in the main text – sulfate controls ALWC but pH is buffered.

ALWC in LA was highest near the coast, where RH and SO_4^{2-} concentrations were elevated, and decreased progressively inland as RH declined. This RH-driven gradient in ALWC, without a corresponding gradient in pH, provides a within-city illustration of the ALWC–pH decoupling described in Sect. 3.2.2 of the main text.

S2.2.4. California San Joaquin Valley – Urban–Rural Contrast with Los Angeles

The California San Joaquin Valley (SJV) flight provided a rural reference environment under meteorological conditions (temperature, RH) comparable to those in LA, enabling a direct urban–rural compositional comparison. The SJV was not impacted by smoke during the campaign sampling periods used in this analysis.

The most distinctive feature of the SJV relative to LA was the substantially higher TNH_x (approximately twice that of LA), consistent with the dominance of agricultural NH_3 sources – fertilizer application, livestock operations, and irrigation-driven volatilization – that characterize California's agricultural intensive region. Despite this elevated TNH_x, mean PM_1 was lower in the SJV than in LA due to lower OA and NO_3^- mass. TNO_3 in the SJV (~4.4 μg m^{-3}) was approximately half that observed in LA, consistent with lower vehicular NO_x concentrations (Table S1). Aerosol-phase nitrate partitioning was similar between LA and the SJV ($\varepsilon(NO_3^-)$ = 22 ± 14% and 20 ± 17%, respectively), indicating that differences in total nitrate loading, not pH, drove the compositional contrast.

Predicted pH in the SJV was comparable to that in LA despite the substantially elevated TNH_x. This result is consistent with the NH_3/NH_4^+ buffering mechanism: although NH_3 concentrations were elevated in the SJV, the lower ALWC relative to LA limited NH_3 dissolution into the aerosol phase, offsetting the pH-raising effect of the higher gas-phase NH_3 reservoir. The net result was a pH similar to that of the adjacent urban environment, illustrating the thermodynamic self-regulation of aerosol acidity even under conditions of substantially elevated base concentrations.

S2.3. Spatial Variability Under Smoke-Impacted Conditions

All East Coast flights over NYC, CHI, and Toronto (TO) were smoke-impacted, with the exception of the two low/no-smoke flights discussed above. As detailed in the main text (Sects. 3.1 and 3.2.2), wildfire smoke substantially elevated OA while leaving inorganic species concentrations largely unchanged. This asymmetric compositional smoke characteristic was also reflected in the within-city spatial distributions: OA concentrations showed clear spatial structure associated with smoke plume geometry, while sulfate, nitrate, and ammonia remained relatively spatially uniform across each metropolitan domain.

S2.3.1. New York City – Smoke Conditions (Fig. S10)

During the two smoke-impacted flights over NYC (July 28 and August 9), OA was significantly elevated east of Long Island and the New Haven, Connecticut corridor relative to the metropolitan area, consistent with smoke forecasts predicting higher concentrations in these downwind locations. The spatial enhancement in OA tracked the acetonitrile (CH_3CN) biomass burning tracer, confirming its smoke origin. In contrast, other aerosol species (SO_4^{2-}, NH_4^+, NO_3^-) and gas-phase species (NH_3, HNO_3) remained relatively uniform across the NYC domain during both smoke flights, consistent with the campaign-wide finding that smoke did not systematically perturb inorganic aerosol loading (Sect. S5).

ALWC under smoke conditions in NYC was lower on average than during the high-RH low/no-smoke flight of August 16 (~3.1 vs. 10.3 μg m^{-3}), reflecting the substantially lower RH during the smoke flights. The OA water contribution increased under smoke (to ~50% of total ALWC from ~31% under low/no-smoke) but was insufficient to compensate for the lower inorganic water uptake at reduced RH. Within the smoke-impacted flights, ALWC showed some spatial correlation with OA, particularly in areas of elevated smoke concentration, but the spatial pH field remained constrained near 1.5–2.0 across the flight domain with no systematic spatial structure attributable to the smoke OA gradient.

S2.3.2. Chicago – Smoke Conditions (Fig. S11)

During the four smoke-impacted flights over Chicago (August 1, 2, 8, and 15), OA was particularly elevated over Lake Michigan and its eastern shoreline, where smoke was forecast to persist and lake breezes may have contributed to local accumulation. OA remained elevated throughout the broader metropolitan area during August 1–2, when smoke influence was most intense. Gas-phase HNO_3 was also somewhat elevated over Lake Michigan relative to inland areas, and SO_4^{2-}, NH_4^+, and NH_3 were consistently higher north of the urban core, consistent with the known spatial patterns of industrial and traffic sources in the northern metropolitan area and the prevailing southwesterly flow that advected these emissions northward.

ALWC under smoke conditions in CHI was highest on average among the three smoke-impacted cities (mean 5.98 ± 11.96 μg m^{-3}), driven by the elevated total PM_1 (~3× relative to low/no-smoke conditions) and similar RH. Over Lake Michigan, ALWC was slightly elevated relative to inland areas, consistent with the higher RH and PM_1 loading there. These local ALWC enhancements over the lake were not accompanied by systematic pH depressions, confirming the buffering result at the within-city scale. Predicted pH across the CHI metropolitan domain ranged from approximately 2.0 to 2.5 during smoke conditions, with slightly elevated values (approaching 2.5–3.0) north of the city where TNH_x was higher.

S2.3.3. Toronto and Southern Ontario – Urban–Rural Contrast Under Smoke Conditions (Fig. S12)

Toronto (TO) was sampled exclusively under smoke conditions (August 4 and 5), providing no low/no-smoke baseline for urban comparison. The Southern Ontario (SON) rural region, sampled en route to/from Toronto, provides a contrast environment under the same broad smoke influence.

The most striking compositional contrast between SON and TO was TNH_x, which was approximately three times higher in SON, consistent with agricultural NH_3 sources in the intensively farmed region south and west of Toronto. PM_1 NO_3^-, SO_4^{2-}, and OA were 1.5–2× higher in SON than in TO, and TNO_3 was comparable between the two regions, but $\varepsilon(NO_3^-)$ was approximately twice as high in SON (~40% vs. ~20%), indicating greater aerosol-phase nitrate partitioning in the rural environment despite similar total nitrate loading. This elevated $\varepsilon(NO_3^-)$ in SON is consistent with the higher pH in that region (2.5–3.0 vs. 1.8–2.2 in TO), which shifts the HNO_3/NO_3^- equilibrium toward the particle phase.

The higher pH in SON relative to TO is the clearest example in the AEROMMA dataset of agricultural NH_3 partially overcoming the thermodynamic buffering that maintained pH near 2 across the urban regions. However, even in SON, pH remained below 3 – well within the acidic range – illustrating the limits of NH_3-driven pH elevation described in Sect. 4.1 of the main text. ALWC in SON was proportionally higher than in TO, consistent with the higher inorganic PM_1 and RH, and OA contributed ~65% of total ALWC in TO (the highest OA LWC fraction in the dataset) due to the elevated smoke OA mass in that environment.

S2.4. A Note on Aircraft Sampling

Sampling representativeness. The airborne boundary layer sampling at ~700 m altitude provides a spatially integrated view of the urban boundary layer composition, which may differ from ground-level concentrations at specific emission hotspots. The within-city variability documented here is therefore a lower bound on the true spatial heterogeneity of ALWC and pH across the urban domain. Ground-based network measurements at higher spatial resolution, or lower-altitude aircraft sampling, would be required to characterize the full spatial range of these thermodynamic quantities at the surface.

S3: Comparison of PM_1 Mass Concentration to Measured Particle Volume and Sensitivity of Thermodynamic Model to K^+

S3.1. AMS Mass and Density Correction

A comparison between UHSAS volume measurements to total PM_1 (AMS + SP2 rBC) across all AEROMMA urban flights is shown in Fig. S1. The slope is 2.01, which is the estimated average particle density in g cm^{-3}. This value is substantially higher than the nominal density typically assumed for atmospheric aerosols (~1.4 g cm^{-3}) (Kannosto et al., 2008; Seinfeld and Pandis, 2016), suggesting that as the largest component of PM_1 mass, AMS mass concentrations may be biased high. To assess the impact of this potential bias on model predictions, thermodynamic calculations were repeated using density-corrected AMS inputs (correction factor = 0.67 = 1.4/2.1, i.e., all AMS data multiplied by this factor). Applying the density correction decreased predicted ALWC by approximately 40% but had minimal impact on predicted pH. This translates to an uncertainty in a systematic bias of approximately +40% in predicted ALWC, while pH predictions are relatively insensitive to this correction. Despite the possible concentration bias, the thermodynamic model performance based on nitrate partitioning comparisons was worse with density-corrected inputs than with uncorrected AMS data, (see Figs. S2 and S3). This suggests that the density correction reduces thermodynamic consistency between particle-phase and gas-phase measurements when used jointly as model inputs and may reflect a combination of systematic biases with both the AMS and gas phase species, or that applying a correction factor based on an assumed constant particle density leads to a random uncertainty that affects the thermodynamic predictions.

S3.2. K^+ Sensitivity Tests

Potassium (K^+) is a non-volatile cation (NVC) emitted from biomass burning and can be internally mixed within PM_1, particularly during smoke-impacted periods. To assess its influence on model predictions, sensitivity tests were conducted by varying K^+ inputs from 1% to 100% of NH_4^+ mass concentration. Across all K^+ levels tested, model predictions diverged sharply from observations and the base case (without K^+). Even at K^+ levels as low as 1% of NH_4^+ mass (mean K^+ = 0.005 μg m^{-3}; note: PILS lower limit of detection = 0.01 μg m^{-3}), the model predicted nearly all nitric acid in the particle phase and overestimated $\varepsilon(NH_4^+)$ by a factor of two (Fig. S13), contrary to observations. This behavior was consistent across all K^+ concentrations tested and across all cities, suggesting that K^+ alone, without a corresponding balancing anion, is not a physically realistic model input for these conditions.

S3.3. KCl Sensitivity Tests

Potassium is primarily emitted as KCl from biomass burning, though its concentrations can vary with fire conditions (Lee et al., 2010). To better represent this, Cl^- was included alongside K^+ in additional sensitivity tests, with KCl concentrations ranging from 5% to 100% of NH_4^+ mass concentration. Given that the smoke sampled during AEROMMA was primarily aged, Cl^- was

likely depleted through heterogeneous reactions (Schlosser et al., 2017). Two cases were therefore tested: (i) K:Cl molar ratio = 1 (no Cl depletion) and (ii) K:Cl = 2 (partial Cl depletion). As the model operates in forward mode, total Cl (gas + aerosol) is required as input; in the absence of HCl measurements, an HCl/Cl^- molar ratio of 10 was assumed based on prior smoke observations (Rivera-Adorna et al., 2025). Across all KCl concentrations tested, predictions were substantially closer to observations and the base case, unlike to K^+-only simulations (Fig.s S14 -S17). For the same KCl concentration, cases with Cl depletion showed better agreement with observations than those without. Among all cases tested, KCl at 50% of NH_4^+ with Cl depletion yielded the best match to observed ammonia partitioning across all cities (Fig. S16 and S17), with slopes near unity and correlations exceeding 0.7 in smoke-impacted cities. However, this case still overpredicted aerosol-phase nitrate, showing no improvement in model performance over the base case. Additionally, sensitivity tests using median PILS-measured K^+ from each smoke-impacted flight as direct model inputs showed minimal effect on partitioning predictions (Fig. S18), with results similar to the base case.

S3.4. Cl^- as a Surrogate for Missing Anions

The persistent $\varepsilon(NO_3^-)$ overprediction across all sensitivity tests suggests the possible presence of a missing anion in the thermodynamic model that is not accounted for in the current input dataset. One candidate is organic acids associated with ammonium. To provide a preliminary estimate of this effect, Cl^- was used as a surrogate anion in the form of NH_4Cl, scaled to 5% and 50% of NH_4^+ molar concentration, with HCl assumed to be 10 times the Cl^- concentration. At low Cl^- levels (5%), predicted ammonia and nitrate partitioning was unchanged from the base case. At higher levels (50%), $\varepsilon(NO_3^-)$ again showed no improvement in the bias, whereas $\varepsilon(NH_4^+)$ was overestimated by 40% on average (Fig. S19). Overall, the addition of Cl^- did not substantially improve model performance, suggesting that chloride – and by extension, organic acids with similar thermodynamic properties – is unlikely to fully explain the observed nitrate bias. A more complete characterization of organic acid concentrations and their thermodynamic properties would be needed to assess this hypothesis further.

S4. Asymmetric ALWC Dependence of NO_3^- and NH_4^+ Air-Equivalent Concentrations

This section provides the derivation supporting the possible causes for an asymmetric sensitivity of NO_3^- and NH_4^+ to aerosol liquid water content (ALWC) discussed in Sect. 4.2 of the main text. The derivation, based on ideal solutions, shows that, when expressed in air-equivalent units, the particle-phase nitrate concentration scales with the square of ALWC (W^2), while the particle-phase ammonium concentration has no explicit W dependence.

Following Guo et al. (2017), and ignoring non-ideality, the aqueous-phase concentrations of NO_3^- and NH_4^+ in equilibrium with their gas-phase precursors are given by the effective Henry's law expressions

$$[\mathrm{NO_3^-}]_{\mathrm{aq}} = \frac{H^*_{\mathrm{HNO_3}}\, p_{\mathrm{HNO_3}}}{[\mathrm{H^+}]_{\mathrm{aq}}} \qquad \text{(Eq. S4.1)}$$

$$[\mathrm{NH_4^+}]_{\mathrm{aq}} = H^*_{\mathrm{NH_3}}\, p_{\mathrm{NH_3}}\, [\mathrm{H^+}]_{\mathrm{aq}} \qquad \text{(Eq. S4.2)}$$

where H^*_{HNO3} (mol L^{-1} atm^{-1}) and H^*_{NH3} (atm^{-1}) are the effective Henry's law constant and p_{HNO3} and p_{NH3} are gas-phase partial pressure (atm) for HNO_3 and NH_3, respectively, and $[H^+]_{aq}$ is the aqueous hydrogen ion concentration (mol L^{-1}). Note the inverse dependence on $[H^+]_{aq}$ for the anion (NO_3^-) and direct proportionality for the cation (NH_4^+).

Converting aqueous concentrations to air-equivalent concentrations (μg m^{-3}) requires multiplying by the aerosol liquid water content W (μg m^{-3}), the species molar mass M_i (g mol^{-1}), and dividing by density of water ($\rho_w = 10^3$ g L^{-1}), which for a general chemical species denoted as *i* is:

$$[i]_{\mathrm{air}} = [i]_{\mathrm{aq}} \cdot \frac{W\, M_i}{\rho_w} \qquad \text{(Eq. S4.3)}$$

Then, the aqueous hydrogen ion concentration is related to its air-equivalent value by:

$$[\mathrm{H^+}]_{\mathrm{aq}} = \frac{[\mathrm{H^+}]_{\mathrm{air}}}{W} \times 10^3 \qquad \text{(Eq. S4.4)}$$

Substituting Eqs. S4.1 and S4.4 into Eq. S4.3, the NO_3^- concentration in air is:

$$\mathrm{NO_3^-} = \frac{H^*_{\mathrm{HNO_3}} \cdot p_{\mathrm{HNO_3}} \cdot W^2 \cdot M_{\mathrm{NO_3^-}}}{\rho_w \cdot [\mathrm{H^+}]_{\mathrm{air}}} \times 10^{-6} \qquad \text{(Eq. S4.5)}$$

Similarly substituting Eqs. S4.2 and S4.4 into Eq. S4.3, the NH_4^+ concentration in air is:

$$\mathrm{NH_4^+} = H^*_{\mathrm{NH_3}} \cdot p_{\mathrm{NH_3}} \cdot [\mathrm{H^+}]_{\mathrm{air}} \cdot \frac{M_{\mathrm{NH_4^+}}}{\rho_w} \qquad \text{(Eq. S4.6)}$$

This shows the asymmetry: air-equivalent NO_3^- scales with W^2, while air-equivalent NH_4^+ has no explicit W dependence. For the anion, the W factor from the aqueous-to-air conversion (Eq. S4.3) compounds with the W introduced through the $[H^+]_{aq} \leftrightarrow [H^+]_{air}$ substitution (Eq. S4.4), producing the quadratic dependence. For the cation, these two W factors cancel, since $[H^+]_{aq}$ appears in the numerator of Eq. S4.2. It should be noted that this analysis assumes ideal solutions, which does not strictly apply to the high concentrations (ionic strength) for fine PM of this study, or in general. This means activity coefficients are not unity and since they also depend on ALWC (i.e., ionic strengths), the precise ALWC dependances may substantially deviate from what is shown above. Nonetheless, the qualitative W^2 vs. no-W scaling remains unchanged.

S5: Low Inorganic PM_1 Species Contributions from Smoke in Urban Environments

To assess the influence of smoke on urban PM_1 chemical species and to characterize the extent to which smoke aerosol is diluted within the urban boundary layer, the fractional contribution of smoke to each PM_1 species was estimated. This was done by utilizing the smoke plumes identified in the free troposphere (Chen et al., 2025), where they are unperturbed by urban surface sources, and using these as a reference for smoke composition after transported from the source region.

A spiral profile over Toronto on August 4 was selected for this analysis, as it was one of the most well defined free-tropospheric smoke plume in the study where the aircraft sampled smoke continuously for approximately two minutes and was the plume nearest to an urban area. Although the smoke was aged, the August 4 Toronto flight was also the most heavily smoke-impacted flight of the campaign, providing a limiting case for evaluating smoke perturbation in an urban environment. The vertical profile was obtained near 43.8° N, 79.2° W at approximately 13:23 local time (Fig. S20f).

Normalized excess mixing ratios (NEMRs; Δ[species]/$\Delta[CH_3CN]$) were calculated for each species with respect to acetonitrile (CH_3CN), a conservative biomass burning tracer, using linear regression analysis of the free-tropospheric smoke plume data, where the regression slopes represent the NEMRs. Boundary layer species concentrations attributable to smoke were then estimated by multiplying the free-tropospheric NEMRs by background-subtracted CH_3CN concentrations measured in the urban boundary layer. Because Toronto was fully covered by smoke during sampling, a smoke-free background could not be determined directly; therefore, a CH_3CN background of 200 ppt was assumed. Dividing these smoke-attributed concentrations by total measured concentrations yields the fractional contribution of smoke to each species.

Among aerosol species, only OA correlated well with CH_3CN in the free troposphere ($R^2 = 0.6$); all inorganic ions yielded R^2 values near zero, indicating no discernible smoke signature. This is visually corroborated by the vertical profiles of species concentrations during this transect (Fig. S20): CH_3CN and PM_1 OA were markedly elevated in the free troposphere relative to the boundary layer, while PM_1 SO_4^{2-}, TNO_3, and TNH_x showed no corresponding enhancement, consistent with a smoke layer aloft that was compositionally distinct from the urban surface aerosol below. Within the boundary layer, the estimated fractional contribution of smoke to PM_1 OA was approximately 80% on average, indicating that the majority of OA over Toronto during this flight was attributable to biomass burning. In contrast, the negligible correlations for SO_4^{2-}, TNO_3, and TNH_x confirm that these species were predominantly of urban origin and were not systematically enhanced by smoke. This analysis further supports the finding in the main text (Sect. 3.1) that smoke selectively enhanced OA while leaving the inorganic PM_1 system largely undisturbed. It also supports the view that K^+ or KCl, also a minor component of smoke, relative to OA, did not affect the aerosol pH to a discernable extent for this study.

Table S1. Mean ± 1 standard deviation of boundary layer mixing ratios of NO, NO_2, and O_3 (ppbv) measured during AEROMMA, grouped by city and smoke condition. Gray shading indicates smoke impacted locations, and green shading are agricultural regions.

City	New York City	New York City	Chicago	Chicago	Toronto	Southern Ontario	Los Angeles	San Joaquin Valley
Smoke condition	no smoke	smoke	no smoke	smoke	smoke	smoke	no smoke	no smoke
NO (ppbv)	0.31 ± 0.68	0.12 ± 0.12	0.16 ± 0.31	0.28 ± 0.43	0.15 ± 0.29	0.15 ± 0.15	1.96 ± 2.05	0.19 ± 0.085
NO_2 (ppbv)	1.18 ± 2.03	0.50 ± 0.47	0.46 ± 0.44	0.95 ± 0.97	0.42 ± 0.54	0.49 ± 0.42	5.48 ± 3.85	0.84 ± 0.52
O_3 (ppbv)	55.6 ± 9.3	44.7 ± 2.9	47.6 ± 4.6	54.6 ± 15.3	41.4 ± 7.6	41.0 ± 5.7	66.2 ± 19.3	61.0 ± 8.3

Table S2a. Summary of slopes and R^2 values (in parentheses) from linear orthogonal distance regression (ODR; intercept = 0) with ISORROPIA-Lite predicted and measured partitioning fractions [$\varepsilon(NH_4^+)$, $\varepsilon(NO_3^-)$] and individual gas- and particle-phase species concentrations (NH_3, NH_4^+, HNO_3, NO_3^-) under low/no-smoke and smoke conditions. Results are shown for the base case, which includes Organic Aerosol (with OA) contributions, and three sensitivity cases–excluding organic aerosol (without OA), reduced relative humidity (RH × 0.85), and increased temperature (T + 0.5 K). In each sensitivity case, only the noted parameter is changed from the base case. The percentage change in slopes relative to the base case is provided in Table S2b.

Condition	Case	NH_3	NH_4^+	$\varepsilon(NH_4^+)$	HNO_3	NO_3^-	$\varepsilon(NO_3^-)$
Low/no-smoke	Base: with OA	0.99 (1.00)	1.07 (0.97)	1.06 (0.96)	0.92 (0.97)	1.28 (0.97)	1.31 (0.84)
	Without OA	1.02 (1.00)	0.86 (0.96)	0.94 (0.96)	0.80 (0.98)	0.87 (0.92)	1.00 (0.82)
	RH x 0.85	1.01 (1.00)	0.94 (0.98)	0.95 (0.96)	1.01 (0.99)	1.01 (0.97)	0.96 (0.89)
	T +0.5	1.00 (1.00)	1.04 (0.97)	1.05 (0.96)	0.94 (0.98)	1.21 (0.97)	1.23 (0.84)
Smoke	Base: with OA	1.01 (0.99)	1.01 (0.97)	0.99 (0.89)	0.97 (0.99)	1.23 (0.94)	1.31 (0.79)
	Without OA	1.06 (0.99)	0.88 (0.92)	0.89 (0.80)	0.79 (0.98)	0.68 (0.86)	0.69 (0.68)
	RH x 0.85	1.04 (0.99)	0.93 (0.95)	0.93 (0.85)	1.04 (0.99)	0.85 (0.95)	0.85 (0.79)
	T +0.5	1.01 (0.99)	0.99 (0.97)	0.98 (0.89)	0.98 (0.99)	1.16 (0.94)	1.25 (0.79)

Table S2b. Percent difference in slope for the given perturbation relative to the base case derived from the above table, i.e., = (Slope with perturbation – Base slope)/Base Slope x 100%.

Low/no-smoke	Without OA	3%	-20%	-11%	-13%	-32%	-24%
	RH x 0.85	2%	-12%	-10%	10%	-21%	-27%
	T +0.5	1%	-3%	-1%	2%	-5%	-6%
Smoke	Without OA	5%	-13%	-10%	-19%	-45%	-47%
	RH x 0.85	3%	-8%	-6%	7%	-31%	-35%
	T +0.5	0%	-2%	-1%	1%	-6%	-5%

Table S3. Fractional species contributions to PM_1 aerosol liquid water content (ALWC) and PM_1 mass concentration across AEROMMA flight regions, stratified by smoke condition and relative humidity (RH) bin. Gray shading indicates smoke impacted locations, and green shading are agricultural regions. The "% data" column indicates the fraction of observations within each RH bin for a given region and condition, with the corresponding bar providing a visual representation of relative data density. Colored as a continuous heatmap scaled from 0 to 100%, where green indicates lower values and red indicates higher values.

City	Condition	RH	% data	ALWC fraction %				PM1 mass fraction %			
				(NH4)2SO4	NH4NO3	OA		SO42-	NO3-	OA	NH4+
NYC	no smoke	40 - 55 %	1%	87	5	8		39	4	44	13
		55 - 70 %	12%	70	3	27		24	2	65	9
		70 - 85%	86%	58	7	31		20	2	67	8
	smoke	40 - 55 %	44%	34	0	66		6	1	92	2
		55 - 70 %	40%	49	2	48		12	1	82	4
		70 - 85%	15%	42	6	50		11	2	82	4
CHI	no smoke	40 - 55 %	22%	68	2	30		19	2	72	7
		55 - 70 %	44%	58	5	37		16	3	75	6
		70 - 85%	34%	45	12	40		14	4	75	6
	smoke	40 - 55 %	16%	53	5	39		13	2	78	5
		55 - 70 %	57%	50	7	39		13	2	78	6
		70 - 85%	27%	32	17	43		10	4	78	6
TO	smoke	40 - 55 %	24%	35	0	65		6	1	91	2
		55 - 70 %	46%	31	2	67		6	1	91	2
		70 - 85%	30%	28	6	65		6	1	89	3
SON	smoke	40 - 55 %	1%	30	5	65		5	2	91	3
		55 - 70 %	48%	27	7	66		5	1	90	3
		70 - 85%	51%	23	10	66		5	2	90	3
LA	no smoke	40 - 55 %	62%	42	15	38		9	6	78	5
		55 - 70 %	32%	34	37	26		10	15	65	8
		70 - 85%	7%	43	37	19		15	11	54	10
SJV	no smoke	40 - 55 %	73%	60	8	30		16	4	71	8
		55 - 70 %	25%	44	33	22		15	13	60	10
		70 - 85%	2%	43	28	26		15	6	64	10

Table S4. Predicted organic aerosol density (ρ_{OA}) and hygroscopicity parameter (κ_{OA}), and propagation of their uncertainties into organic aerosol liquid water content (OA LWC). Our analyses assumed constant values for $\rho_{\mathrm{OA}}(= 1.3\ \mathrm{g\ cm^{-3}})$and $\kappa_{\mathrm{OA}}(= 0.1)$ to predict OA water by ISORROPIA-Lite. Alternatively, these parameters could be derived from AMS O:C, H:C, and $f_{\mathrm{CO_2}}$ (Kuwata et al., 2011; Duplissy et al., 2011). To assess the effect of our assumed constant values we performed an uncertainty analysis. The table compares the AMS OA mass measurement uncertainty (discussed in Supplement S3) to the uncertainty in using constant OA parameters versus those derived from the AMS OA composition data. Uncertainties in ρ_{OA} and κ_{OA} represent the differences between the predicted and assumed constant values. Total OA LWC uncertainty was calculated by propagating the uncertainties associated with OA mass (38%), RH (15%), ρ_{OA}, and κ_{OA}in quadrature. The contribution of each governing factor to total OA LWC uncertainty was calculated from its fractional contribution. The results are shown for various locations and smoke conditions.

	New York City		Chicago		Toronto	Southern Ontario	LA	San Joaquin Valley
	No smoke	Smoke	No smoke	Smoke	Smoke	Smoke	No smoke	No smoke
Predicted OA properties								
ρ_{OA}, g cm^{-3}	1.40 ± 0.08	1.40 ± 0.04	1.39 ± 0.09	1.43 ± 0.03	1.40 ± 0.03	1.41 ± 0.02	1.29 ± 0.06	1.40 ± 0.05
κ_{OA}	0.12 ± 0.05	0.13 ± 0.02	0.13 ± 0.06	0.15 ± 0.02	0.13 ± 0.02	0.14 ± 0.01	0.09 ± 0.04	0.15 ± 0.04
Uncertainty relative to assumptions								
$\frac{\rho_{OA} - 1.3}{\rho_{OA}}$	7%	7%	6%	9%	7%	8%	-1%	7%
$\frac{\kappa_{OA} - 0.1}{\kappa_{OA}}$	17%	23%	23%	33%	23%	29%	-11%	33%
Propagated OA LWC uncertainty	45%	47%	47%	54%	47%	50%	42%	53%
Contribution of each component to overall OA LWC uncertainty								
AMS OA	72%	64%	64%	50%	64%	57%	81%	51%
RH	11%	10%	10%	8%	10%	9%	13%	8%
ρ_{OA}	3%	2%	2%	3%	2%	2%	0%	2%
κ_{OA}	14%	24%	24%	39%	24%	32%	7%	39%

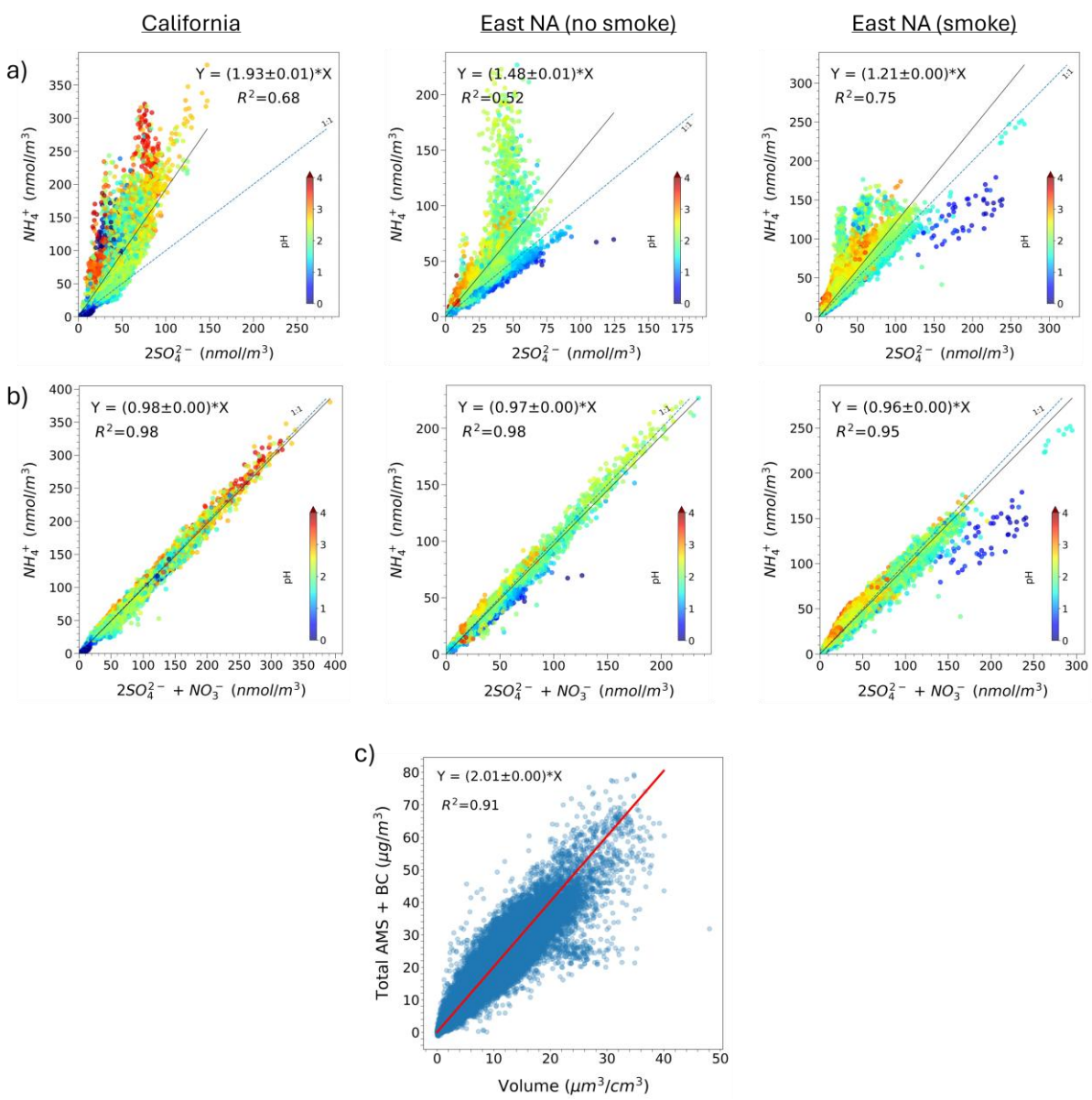

Figure S1. Evaluation of aerosol ion balance and particle density. a) Molar concentrations of NH_4^+ versus $2SO_4^{2-}$, and b) NH_4^+ versus $2SO_4^{2-} + NO_3^-$ for across various locations and conditions. Data points are colored by predicted aerosol pH. Black lines show linear orthogonal distance regression (ODR) fit with intercept set to zero; with with slopes and coefficients of determination (R^2) reported in each panel; blue dotted lines indicate the 1:1 relationship. The closer agreement with the 1:1 line after inclusion of nitrate indicates that nitrate, together with sulfate, accounts for most of the measured ammonium charge. East NA is eastern North America and includes all data over Chicago and east up to and including New York and and Long Island. c) Comparison between Total PM_1 mass (AMS + SP2 rBC) and particle volume measurements for the entire campaign. Data are 1 Hz measurements. Red line represents ODR fit with intercept set to zero; slope and R^2 values are reported. The slope represents the effective PM_1 density (g cm^{-3}).

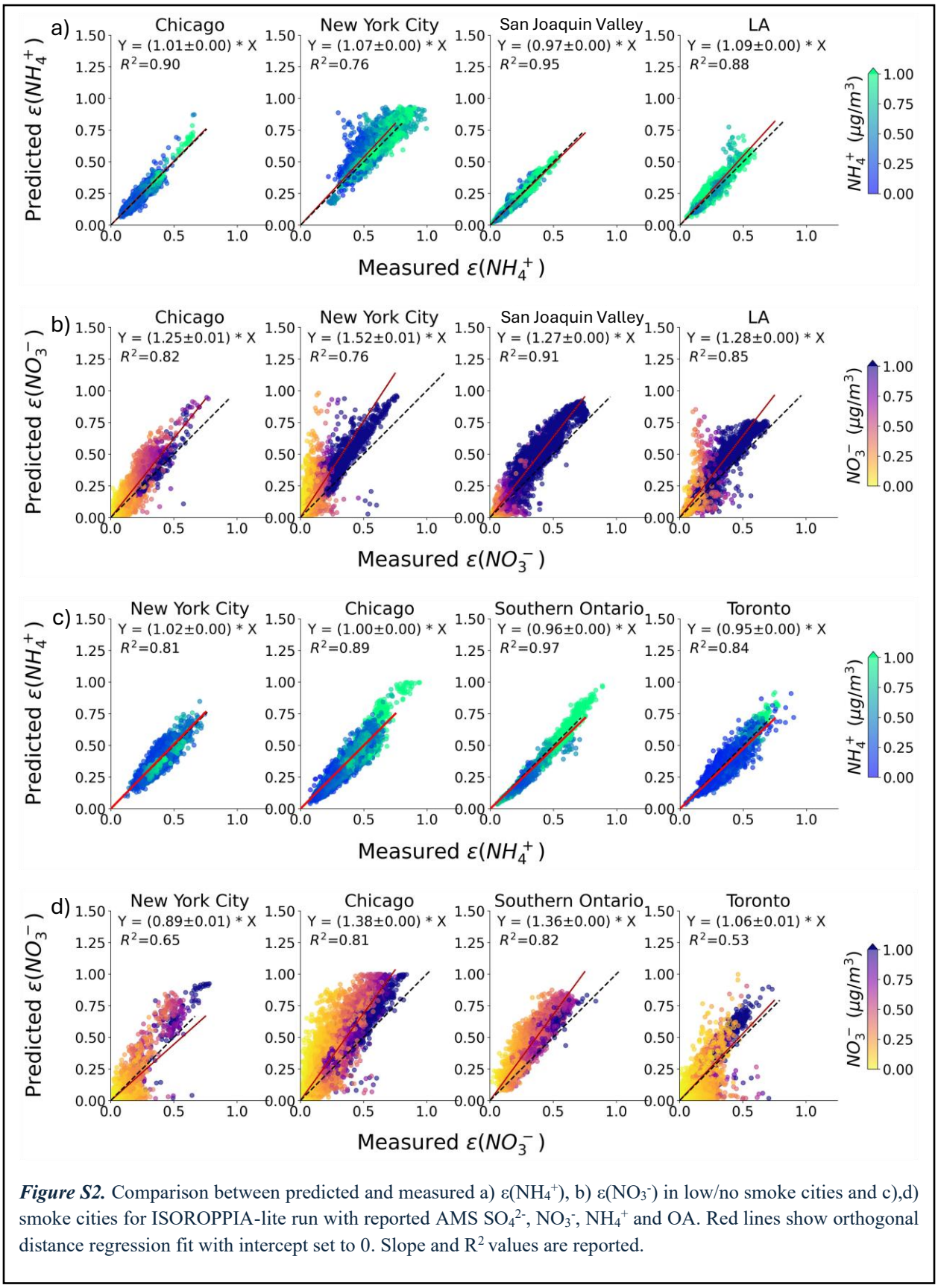

Figure S2. Comparison between predicted and measured a) $\varepsilon(NH_4^+)$, b) $\varepsilon(NO_3^-)$ in low/no smoke cities and c),d) smoke cities for ISOROPPIA-lite run with reported AMS SO_4^{2-}, NO_3^-, NH_4^+ and OA. Red lines show orthogonal distance regression fit with intercept set to 0. Slope and R^2 values are reported.

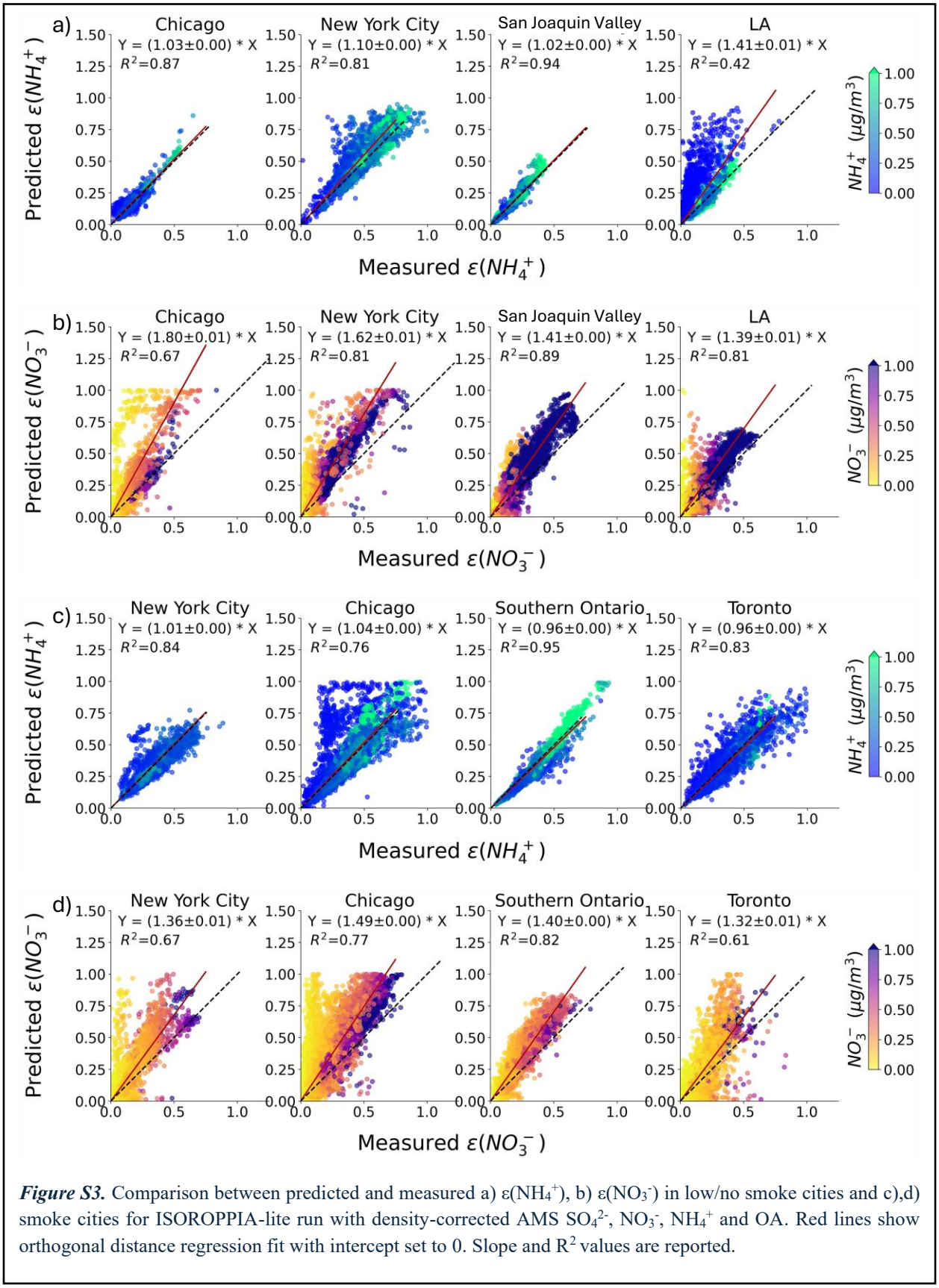

Figure S3. Comparison between predicted and measured a) $\varepsilon(NH_4^+)$, b) $\varepsilon(NO_3^-)$ in low/no smoke cities and c),d) smoke cities for ISOROPPIA-lite run with density-corrected AMS SO_4^{2-}, NO_3^-, NH_4^+ and OA. Red lines show orthogonal distance regression fit with intercept set to 0. Slope and R^2 values are reported.

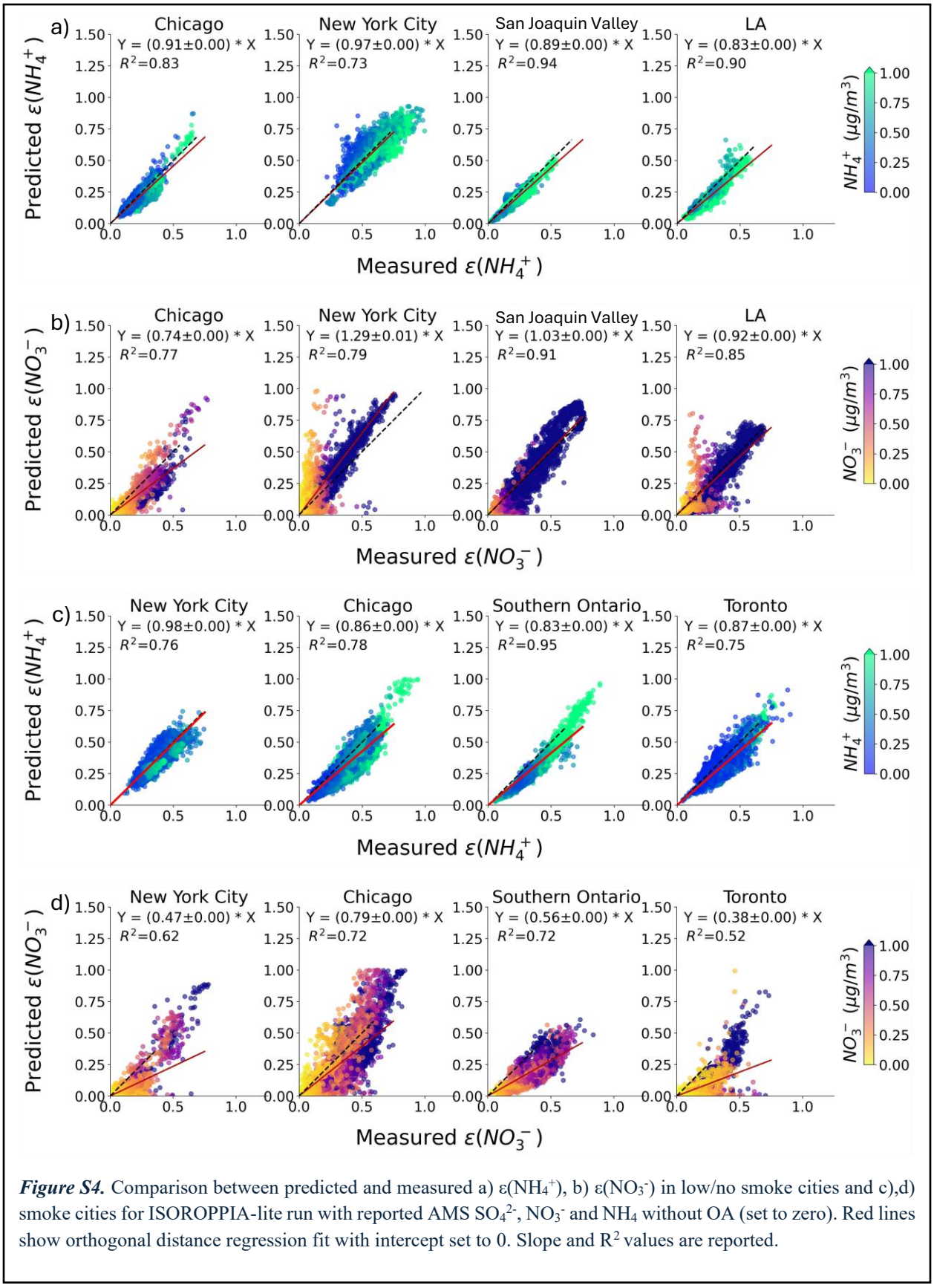

Figure S4. Comparison between predicted and measured a) $\varepsilon(NH_4^+)$, b) $\varepsilon(NO_3^-)$ in low/no smoke cities and c),d) smoke cities for ISOROPPIA-lite run with reported AMS SO_4^{2-}, NO_3^- and NH_4 without OA (set to zero). Red lines show orthogonal distance regression fit with intercept set to 0. Slope and R^2 values are reported.

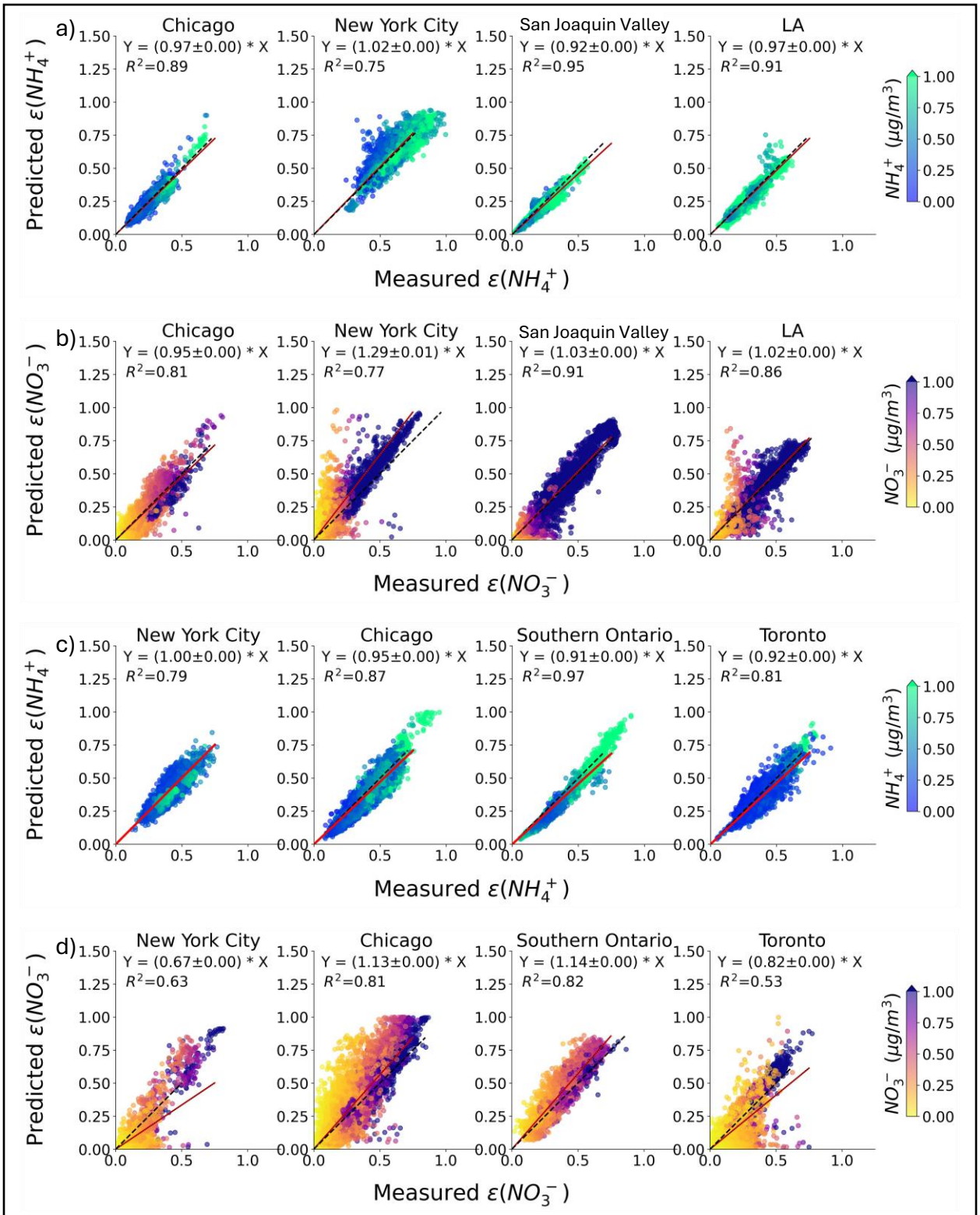

Figure S5. Comparison between predicted and measured a) $\varepsilon(NH_4^+)$, b) $\varepsilon(NO_3^-)$ in low/no smoke cities and c),d) smoke cities for sensitivity test with NH_3 and HNO_3 reduced by 1x uncertainty. Red lines show orthogonal distance regression fit with intercept set to 0. Slope and R^2 values are reported.

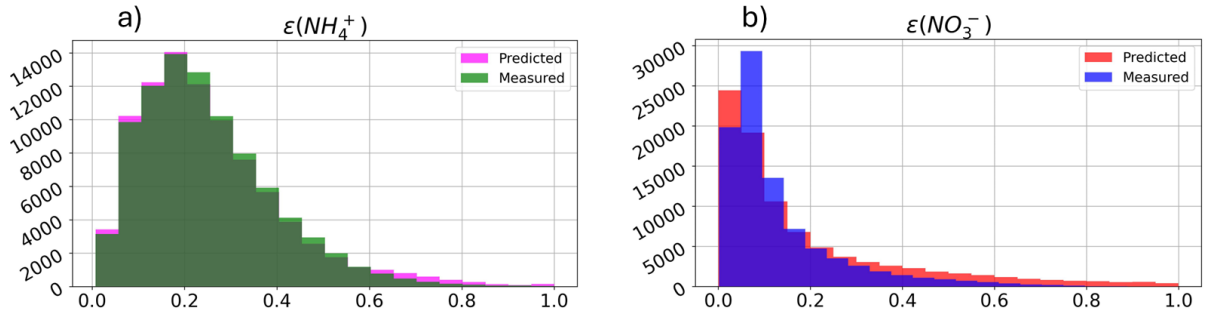

Figure S6. Frequency distributions of measured and ISORROPIA-Lite predicted partitioning coefficients for (a) ammonium [$\varepsilon(NH_4^+)$] and (b) nitrate [$\varepsilon(NO_3^-)$] across all AEROMMA flights.

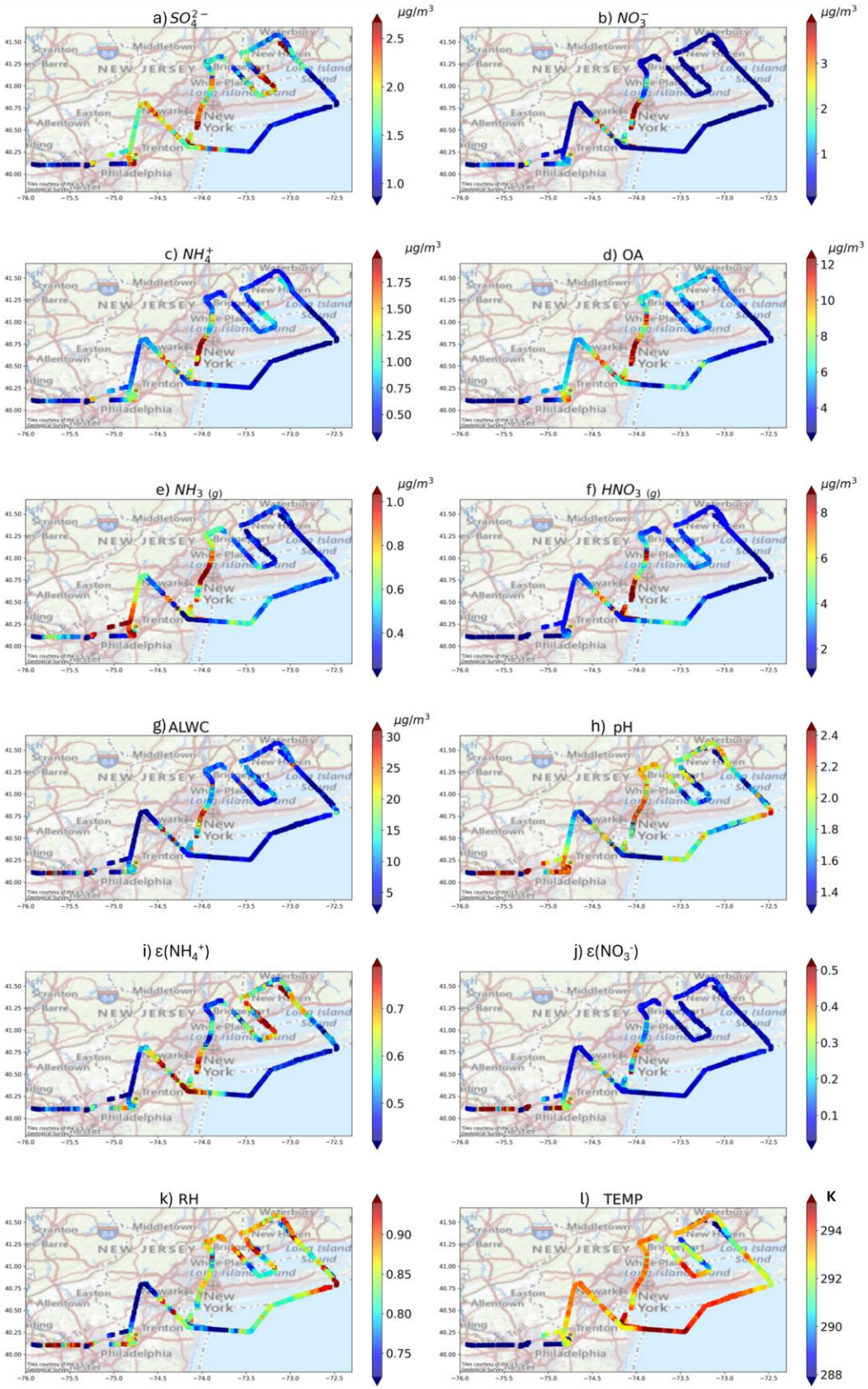

Figure S7. Spatial distributions of PM_1 aerosol species (SO_4^{2-}, NO_3^-, NH_4^+, OA), gas-phase species (NH_3, HNO_3), ISORROPIA-Lite predicted ALWC and pH (with OA contributions), measured partitioning fractions [$\varepsilon(NH_4^+)$ and $\varepsilon(NO_3^-)$], and meteorological parameters (RH and temperature) over the New York City metropolitan area during the August 16 low/no-smoke boundary layer flight. Flight altitude was approximately 700 m except over water bodies where the aircraft descended to ~30 m. The base maps were designed and developed by USGS | Powered by USGS (https://basemap.nationalmap.gov/arcgis/rest/services/USGSTopo/MapServer).

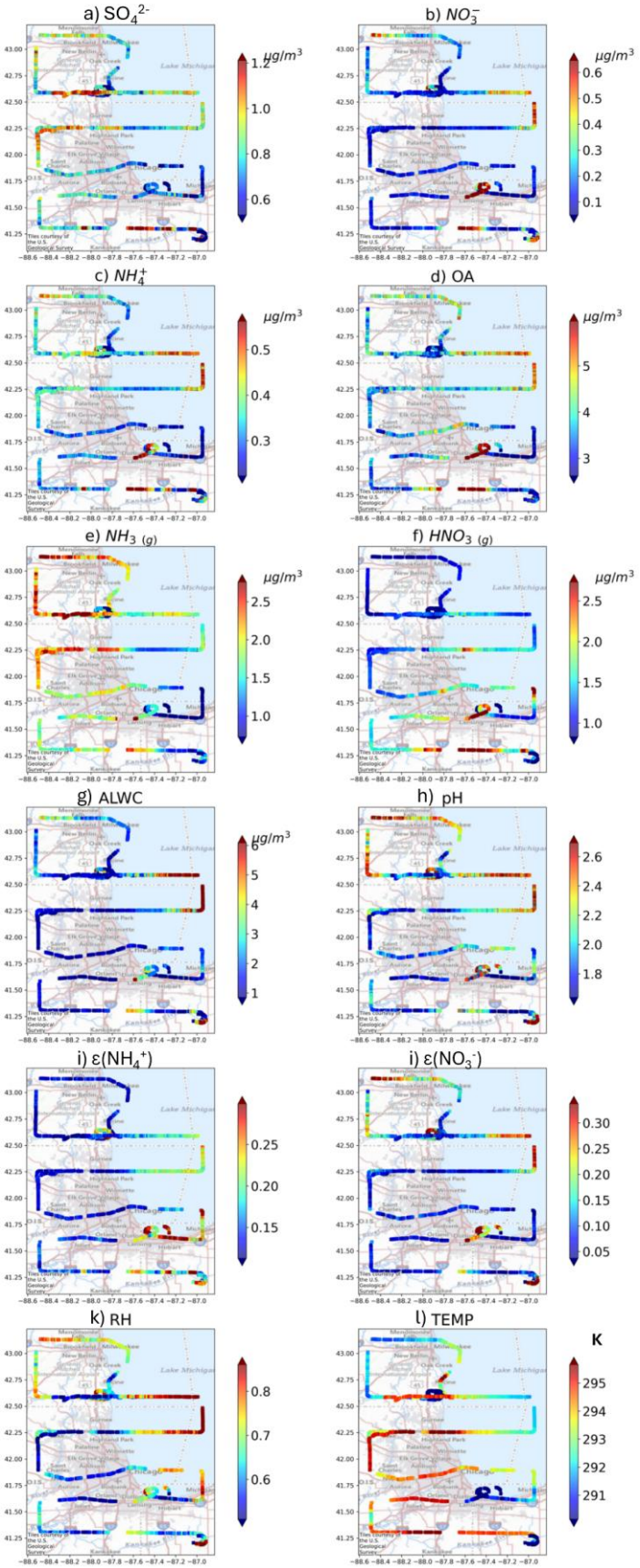

Figure S8. Spatial distributions of PM_1 aerosol species (SO_4^{2-}, NO_3^-, NH_4^+, OA), gas-phase species (NH_3, HNO_3), ISORROPIA-predicted ALWC and pH (with OA contributions), measured partitioning fractions [$\varepsilon(NH_4^+)$ and $\varepsilon(NO_3^-)$], and meteorological parameters (RH and temperature) over Chicago during low/no-smoke flights. The base maps were designed and developed by USGS | Powered by USGS (https://basemap.nationalmap.gov/arcgis/rest/services/USGSTopo/MapServer).

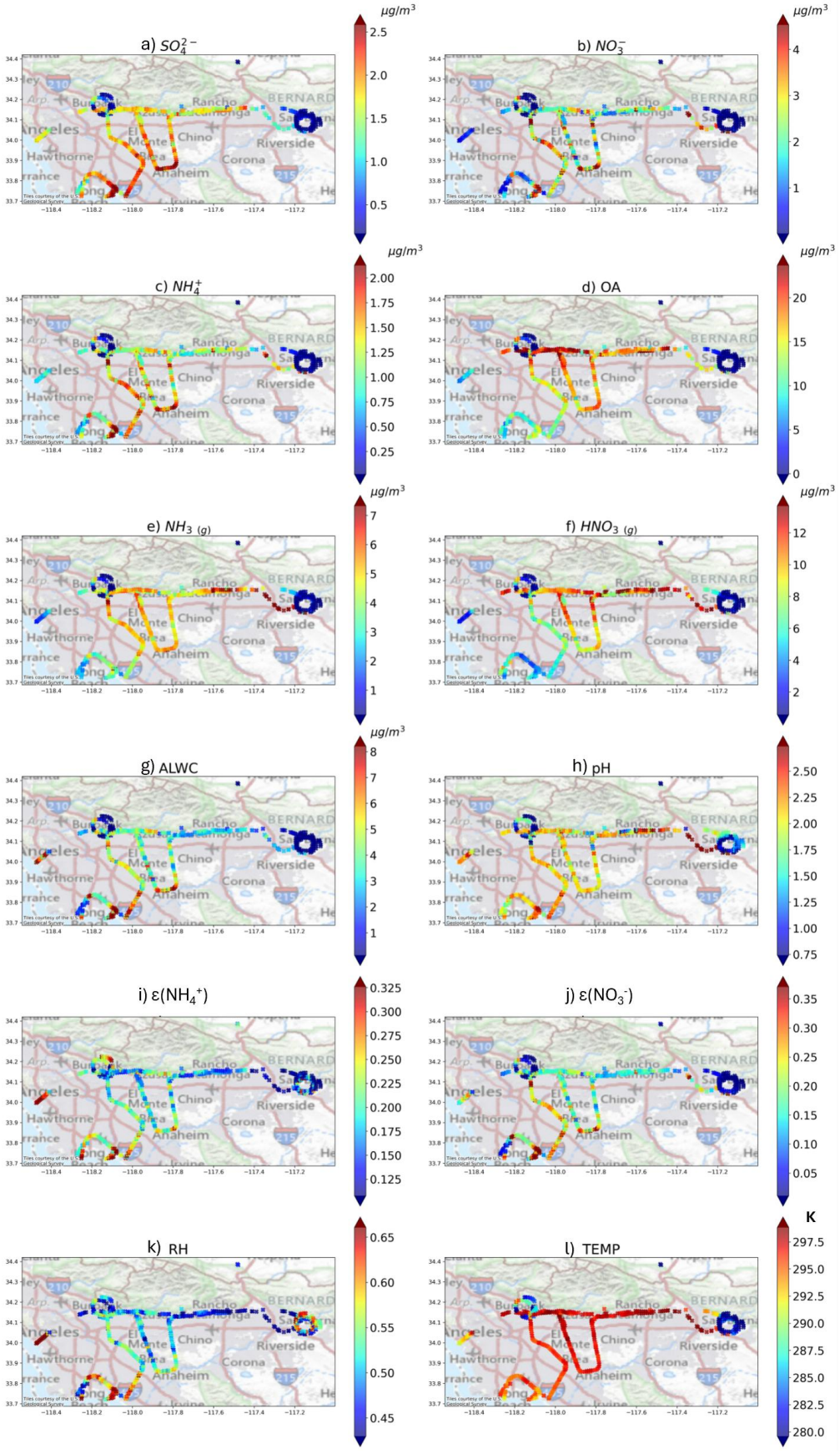

Figure S9. Spatial distributions of PM_1 aerosol species (SO_4^{2-}, NO_3^-, NH_4^+, OA), gas-phase species (NH_3, HNO_3), ISORROPIA-predicted ALWC and pH (with OA contributions), measured partitioning fractions [ε(NH_4^+) and ε(NO_3^-)], and meteorological parameters (RH and temperature) over Los Angeles during low/no-smoke flights. The base maps were designed and developed by USGS | Powered by USGS (https://basemap.nationalmap.gov/arcgis/rest/services/USGSTopo/MapServer).

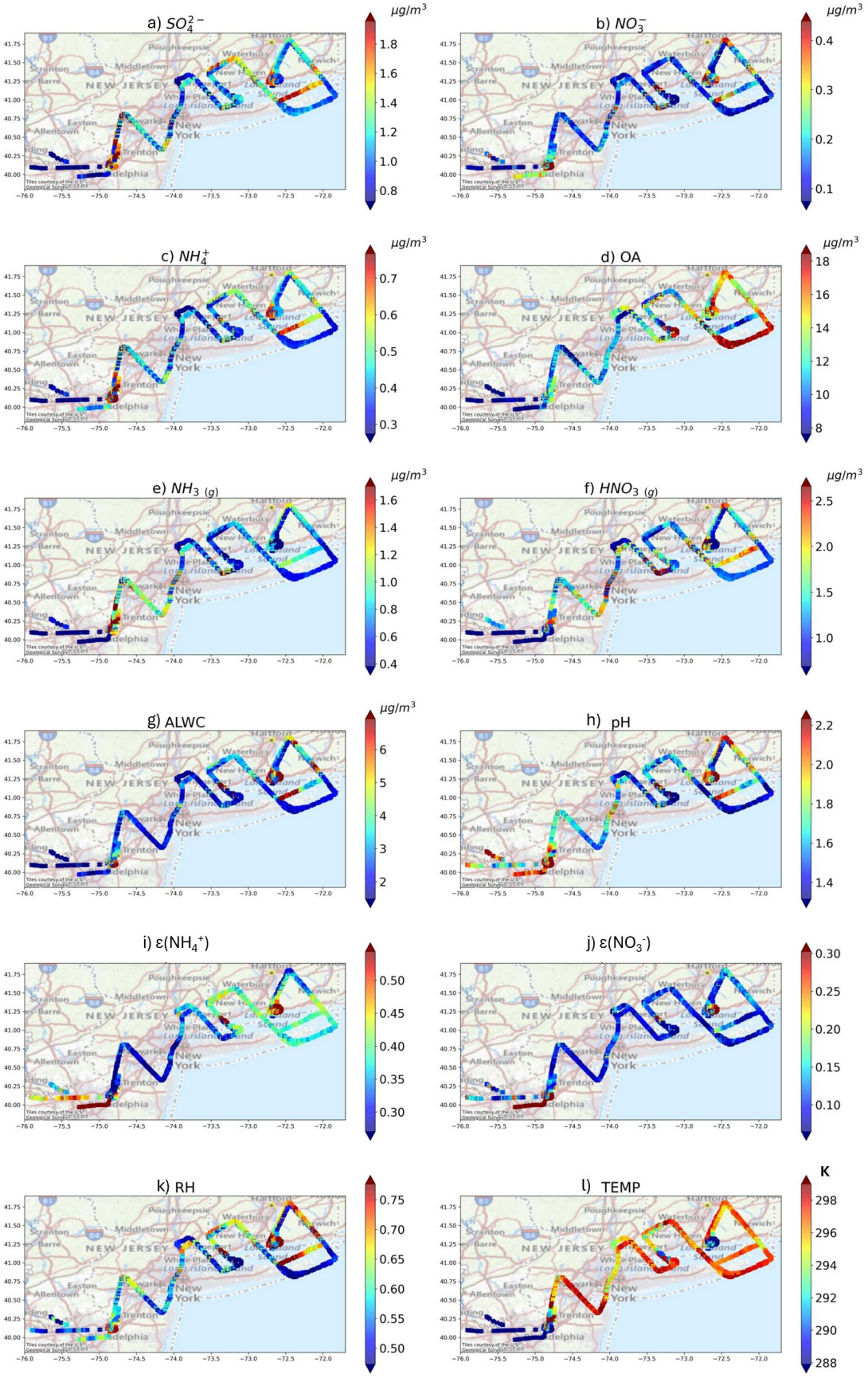

Figure S10. Spatial distributions of PM_1 aerosol species (SO_4^{2-}, NO_3^-, NH_4^+, OA), gas-phase species (NH_3, HNO_3), ISORROPIA-predicted ALWC and pH (with OA contributions), measured partitioning fractions [ε(NH_4^+) and ε(NO_3^-)], and meteorological parameters (RH and temperature) over NYC during smoke flights. The base maps were designed and developed by USGS | Powered by USGS (https://basemap.nationalmap.gov/arcgis/rest/services/USGSTopo/MapServer).

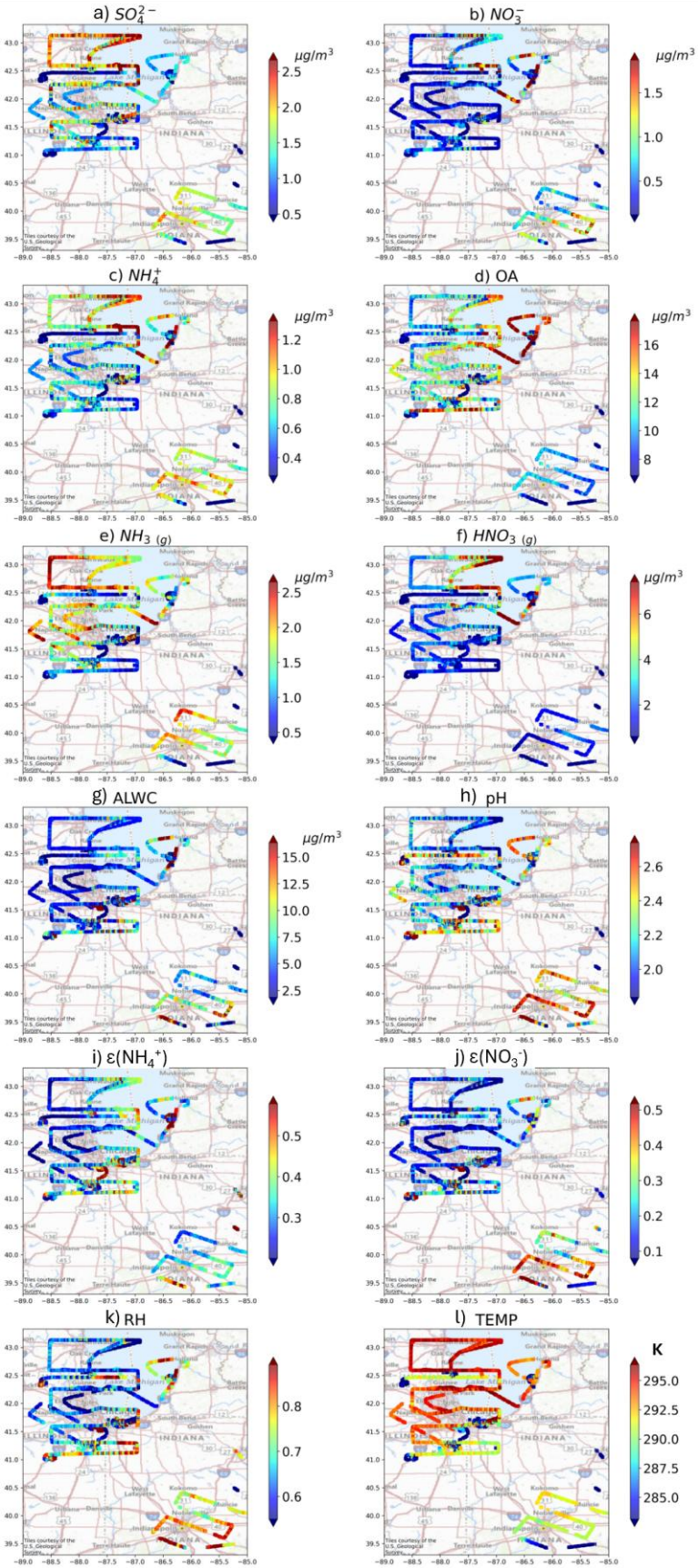

Figure S11. Spatial distributions of PM_1 aerosol species (SO_4^{2-}, NO_3^-, NH_4^+, OA), gas-phase species (NH_3, HNO_3), ISORROPIA-predicted ALWC and pH (with OA contributions), measured partitioning fractions [ε(NH_4^+) and ε(NO_3^-)], and meteorological parameters (RH and temperature) over Chicago during smoke flights. The base maps were designed and developed by USGS | Powered by USGS (https://basemap.nationalmap.gov/arcgis/rest/services/USGSTopo/MapServer).

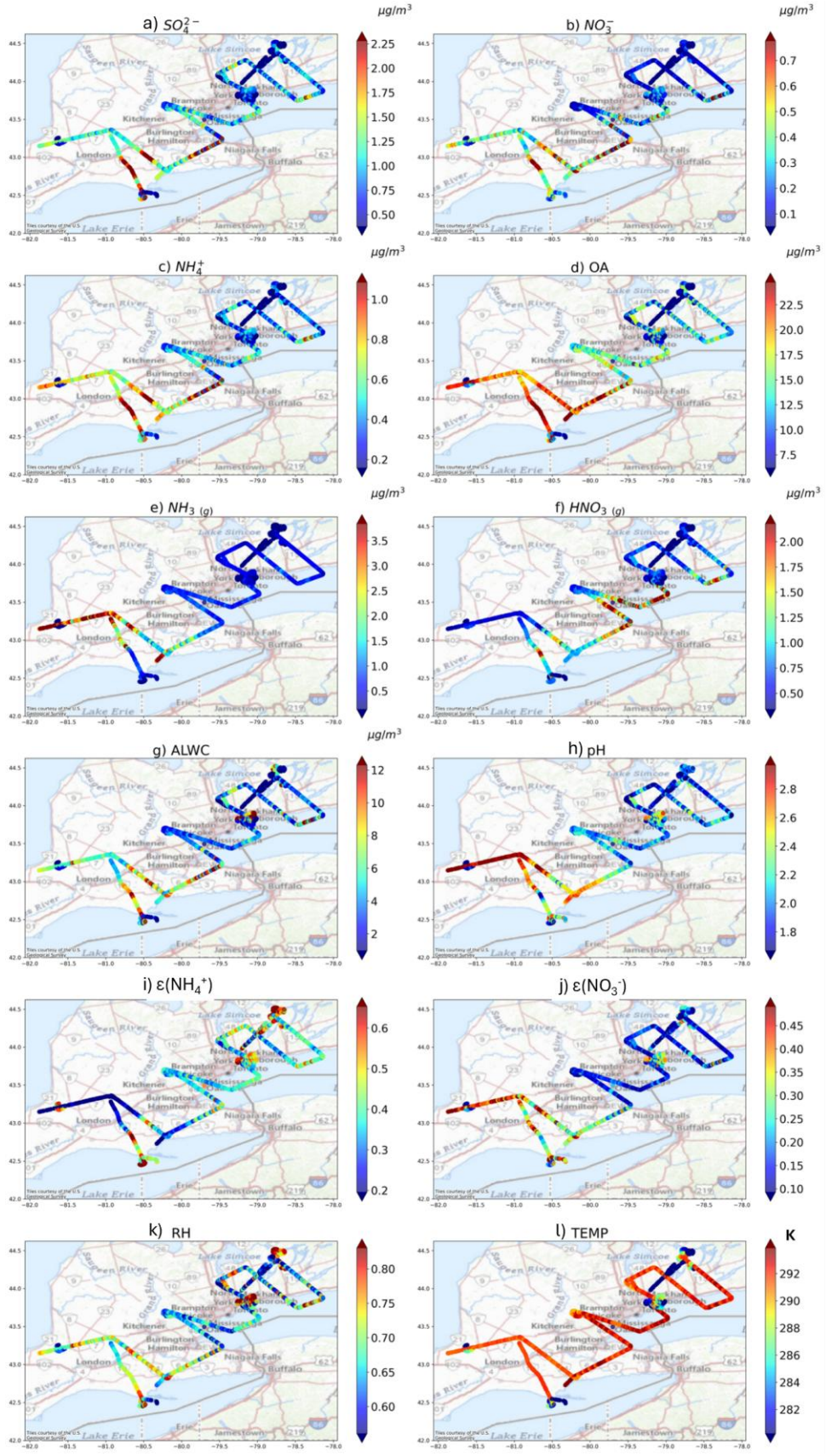

Figure S12. Spatial distributions of PM_1 aerosol species (SO_4^{2-}, NO_3^-, NH_4^+, OA), gas-phase species (NH_3, HNO_3), ISORROPIA-predicted ALWC and pH (with OA contributions), measured partitioning fractions [ε(NH_4^+) and ε(NO_3^-)], and meteorological parameters (RH and temperature) over Toronto during smoke flights. The base maps were designed and developed by USGS | Powered by USGS (https://basemap.nationalmap.gov/arcgis/rest/services/USGSTopo/MapServer).

462

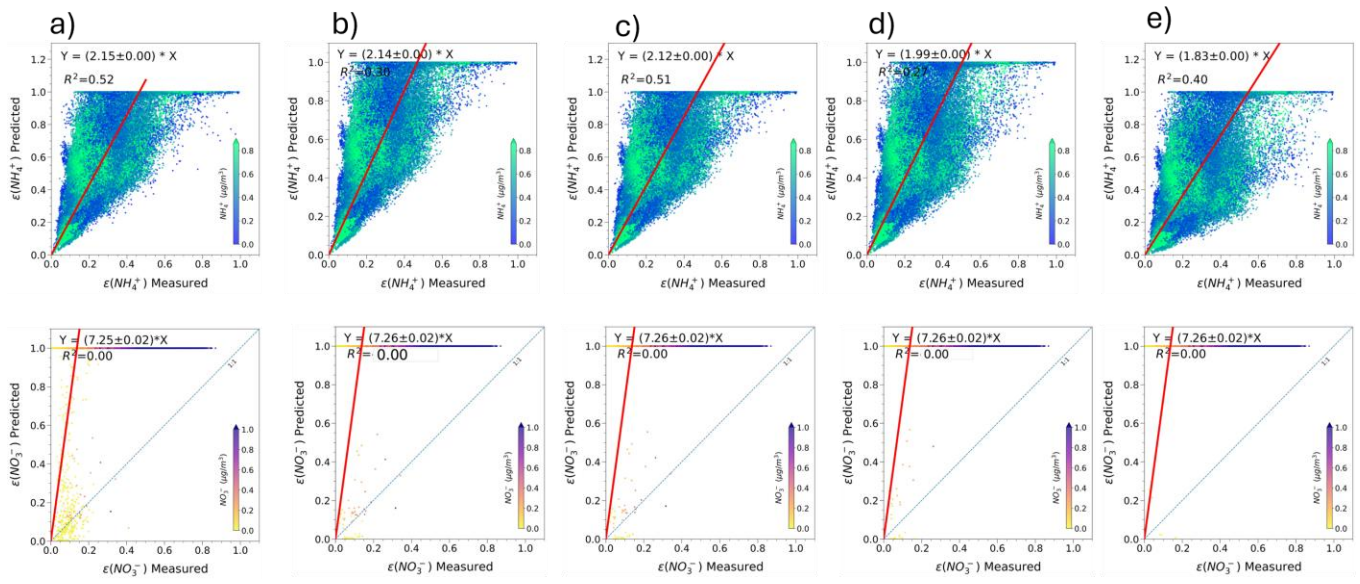

Figure S13. Comparison between predicted and measured ε(NH_4) (top) and ε(NO_3) (bottom) for sensitivity tests with K^+ at a) 1%, b) 5%, c) 10%, d) 50% and e) 100% NH_4^+ mass with adjusted AMS for entire AEROMMA dataset. Red lines represent orthogonal distance regression fit with intercept set to 0. Slope and R^2 values are reported.

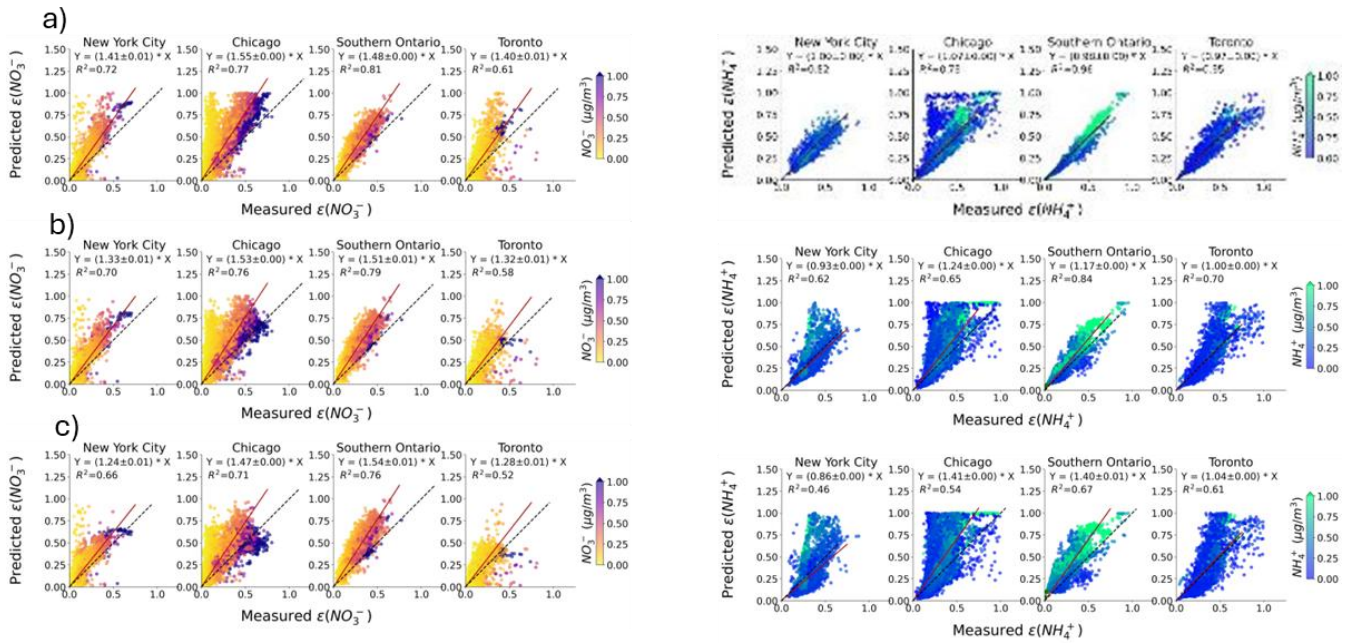

Figure S14. Comparison between predicted and measured ε(NO_3) (left) and ε(NH_4) (right) for sensitivity tests with K^+ at a) 5%, b), 50% and c) 100% NH_4^+ mass and K:Cl molar ratio =1:1 for smoke impacted cities. Red lines represent orthogonal distance regression fit with intercept set to 0. Slope and R^2 values are reported.

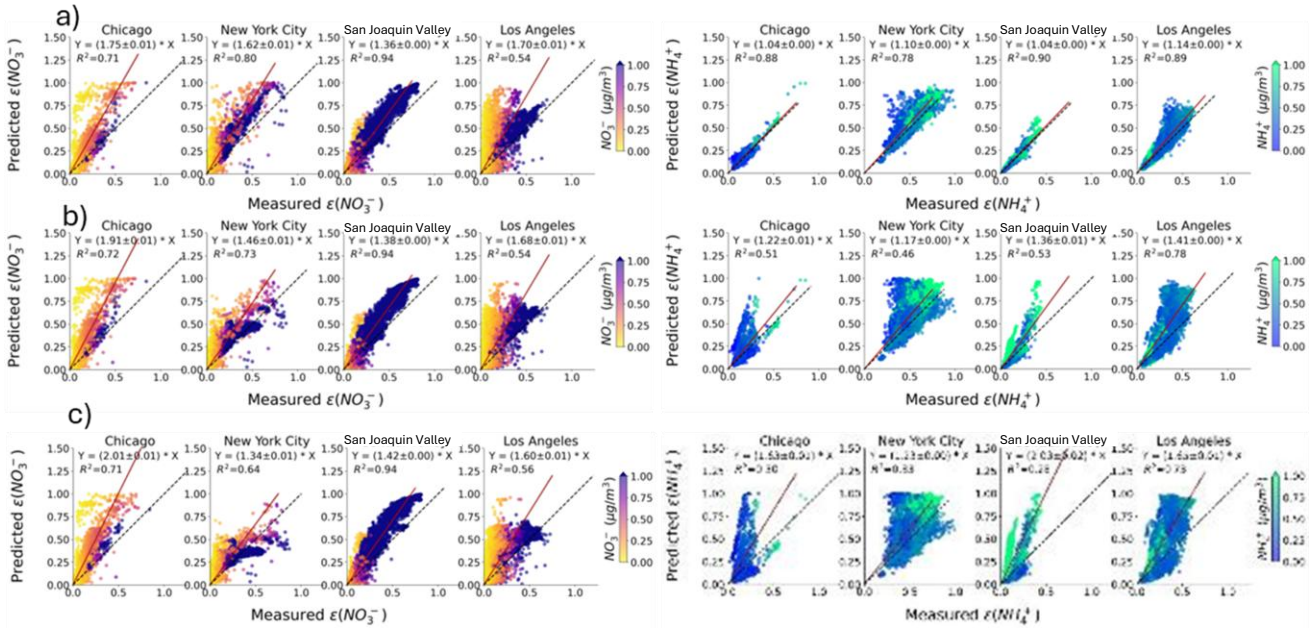

Figure S15. Same a figure S14 but for low/no smoke conditions.

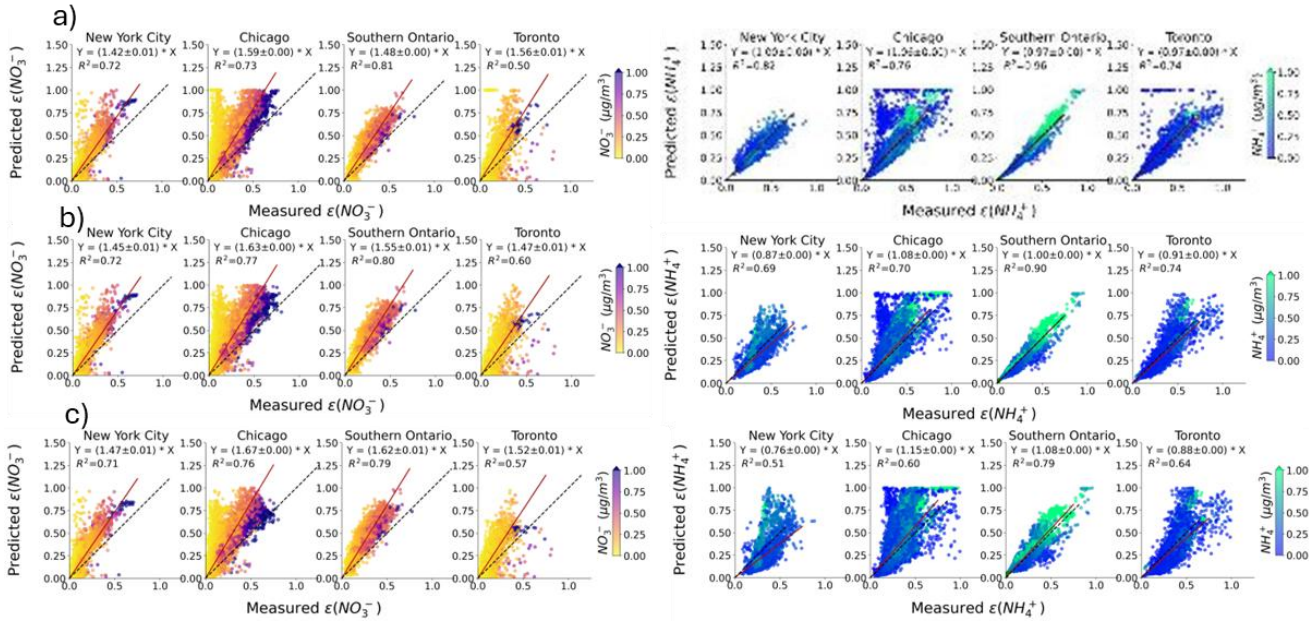

Figure S16. Comparison between predicted and measured $\varepsilon(NO_3)$ (left) and $\varepsilon(NH_4)$ (right) for sensitivity tests with K^+ at a) 5%, b), 50% and c) 100% NH_4^+ mass and K:Cl molar ratio = 2:1 (Cl^- depletion) for smoke impacted cities. Red lines represent orthogonal distance regression fit with intercept set to 0. Slope and R2 values are reported.

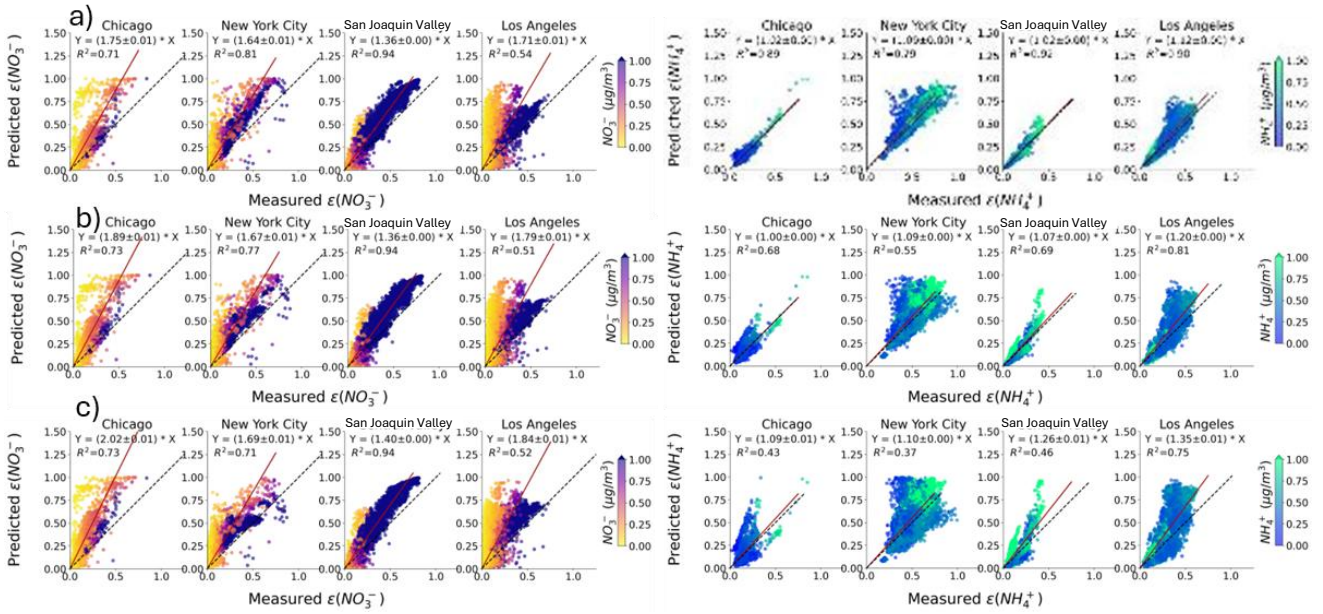

Figure S17. Same a figure S16 but for low/no smoke conditions.

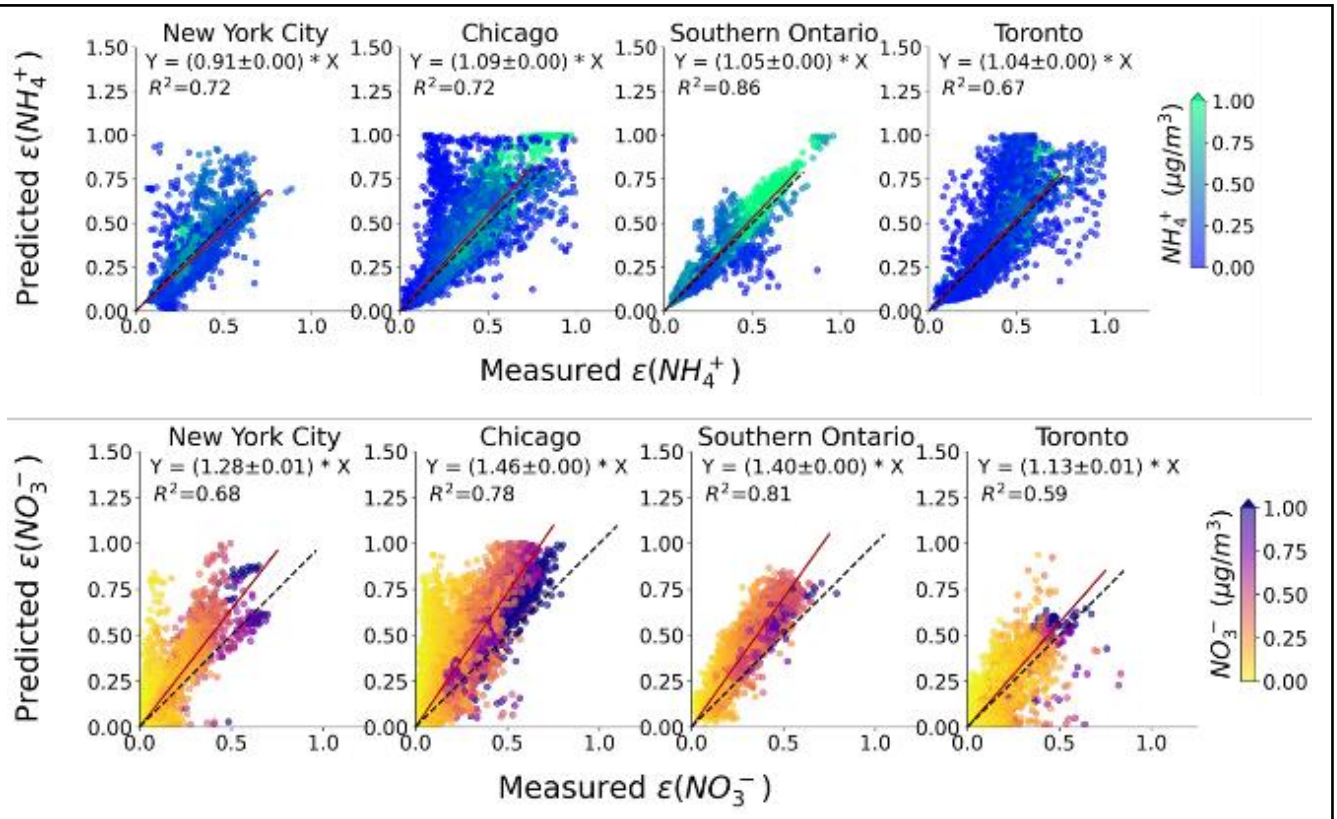

Figure S18. Comparison between predicted and measured ε(NH_4) (top) and ε(NO_3) (bottom) for with median PILS K^+ and K:Cl molar ratio = 1:1 for smoke impacted cities. Red lines represent orthogonal distance regression fit with intercept set to 0. Slope and R^2 values are reported.

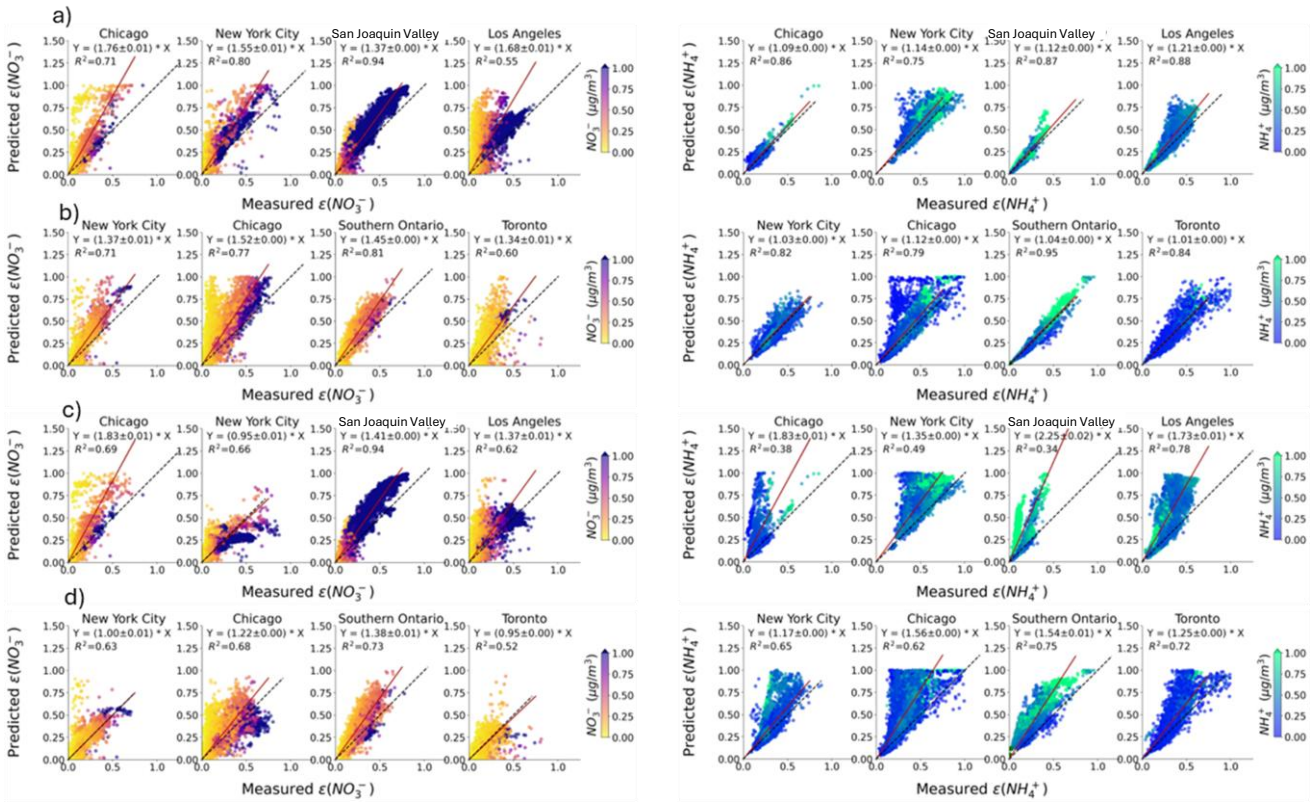

Figure S19. Comparison between predicted and measured $\varepsilon(NO_3^-)$ (left) and $\varepsilon(NH_4^+)$ (right) for sensitivity tests at a) low/no smoke, b), smoke impacted cities with Cl^- = 5% NH_4 and c) low/no smoke, d), smoke impacted cities with Cl^- = 50% NH_4^+. Red lines represent orthogonal distance regression fit with intercept set to 0. Slope and R2 values are reported.

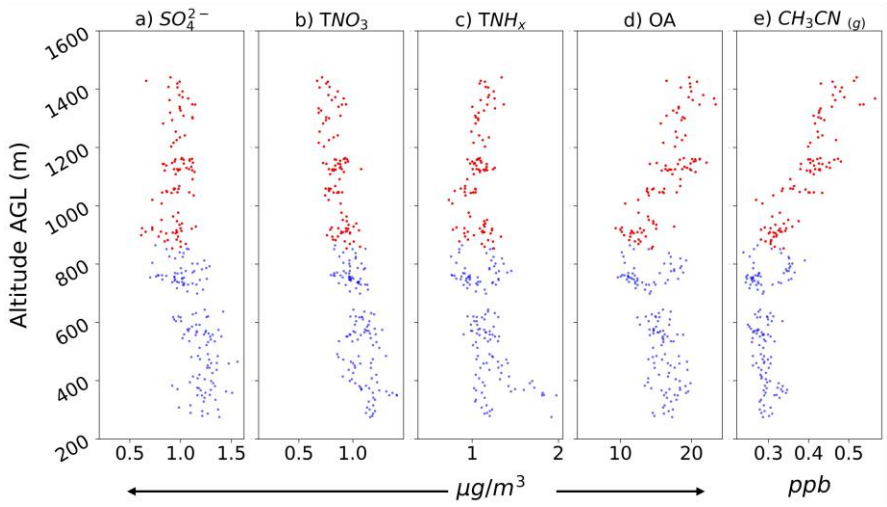

Figure S20. Vertical profiles of (a) SO_4^{2-}, (b) TNO_3, (c) TNHx, (d) OA (in µg m^{-3}), and (e) CH_3CN (in ppbv) during the August 4 spiral profile over Toronto. Panel (f) shows the spiral location over the Toronto metropolitan area. Red points represent the smoke plume. OA and CH_3CN are markedly elevated in the free troposphere relative to the boundary layer, consistent with an aloft smoke layer, whereas inorganic species (SO_4^{2-}, TNO_3, TNHx) show no corresponding enhancement, indicating that the smoke did not substantially perturb the inorganic system. The base maps were designed and developed by USGS | Powered by USGS (https://basemap.nationalmap.gov/arcgis/rest/services/USGSTopo/MapServer).

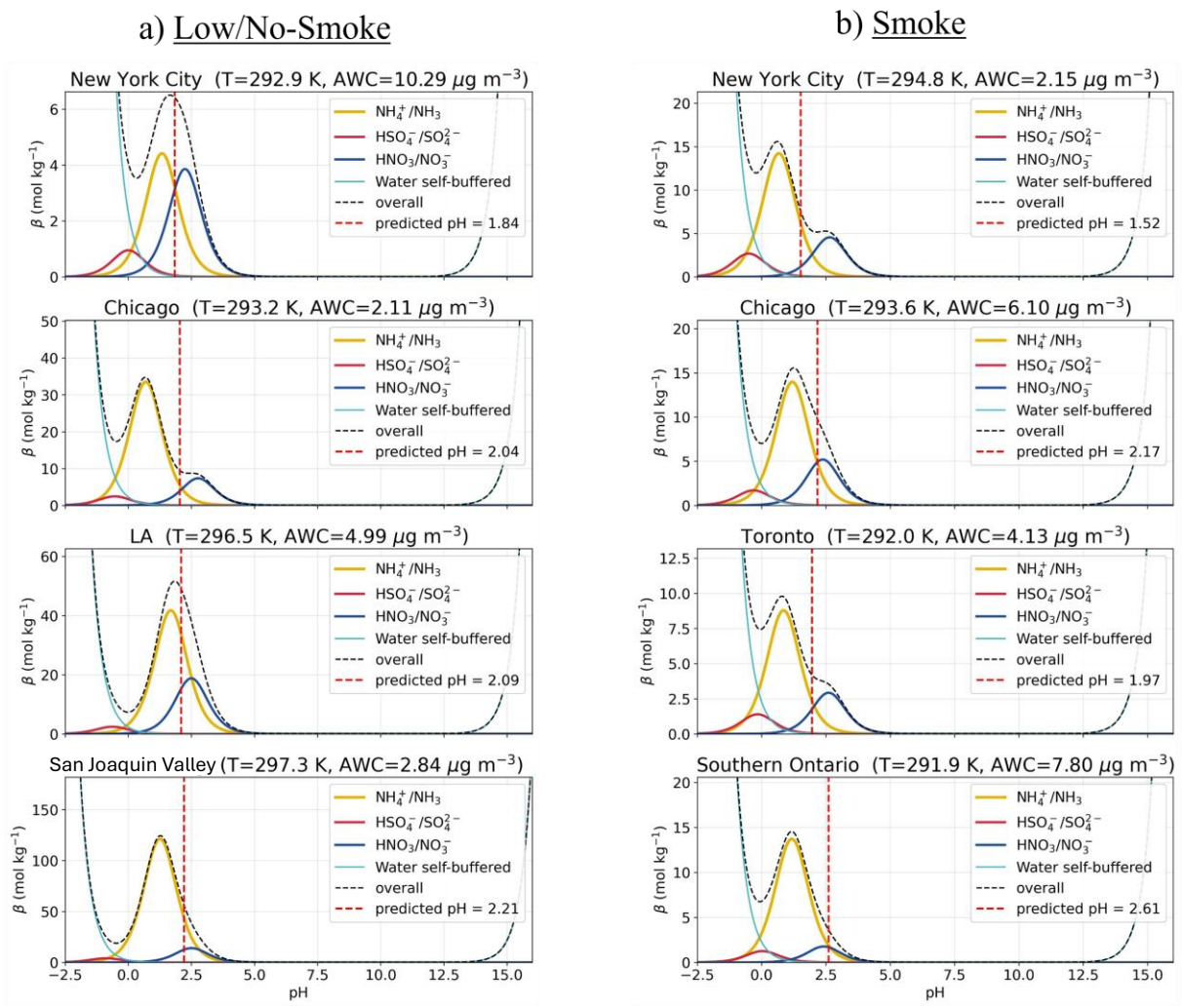

Figure S21. Aerosol pH buffering capacities (β) for the NH_3/NH_4^+, $H_2SO_4/HSO_4^-/SO_4^{2-}$, and HNO_3/NO_3^-systems under the representative temperature (T) and aerosol water content (AWC) shown for each region and smoke condition. The water self-buffering contribution and overall buffering capacity are also shown. Red dashed vertical lines indicate the thermodynamically predicted pH for each case. The overall buffering capacity is dominated by the $NH_3/NH_4^+$and HNO_3/NO_3^- systems near the predicted pH, with their relative contributions varying among regions and smoke conditions.

Reference

Bourgeois, I., Peischl, J., Thompson, C. R., Aikin, K. C., Campos, T., Clark, H., Commane, R., Daube, B., Diskin, G. W., Elkins, J. W., Gao, R.-S., Gaudel, A., Hintsa, E. J., Johnson, B. J., Kivi, R., McKain, K., Moore, F. L., Parrish, D. D., Querel, R., Ray, E., Sánchez, R., Sweeney, C., Tarasick, D. W., Thompson, A. M., Thouret, V., Witte, J. C., Wofsy, S. C., and Ryerson, T. B.: Global-scale distribution of ozone in the remote troposphere from the ATom and HIPPO airborne field missions, Atmospheric Chemistry and Physics, 20, 10611–10635, https://doi.org/10.5194/acp-20-10611-2020, 2020.

Chace, W. S., Womack, C., Ball, K., Bates, K. H., Bohn, B., Coggon, M., Crounse, J. D., Fuchs, H., Gilman, J., Gkatzelis, G. I., Jernigan, C. M., Novak, G. A., Novelli, A., Peischl, J., Pollack, I., Robinson, M. A., Rollins, A., Schafer, N. B., Schwantes, R. H., Selby, M., Stainsby, A., Stockwell, C., Taylor, R., Treadaway, V., Veres, P. R., Warneke, C., Waxman, E., Wennberg, P. O., Wolfe, G. M., Xu, L., Zuraski, K., and Brown, S. S.: Ozone Production Efficiencies in the Three Largest United States Cities from Airborne Measurements, Environ. Sci. Technol., 59, 13306–13318, https://doi.org/10.1021/acs.est.5c02073, 2025.

Chen, J.-H., Puttu, U., Huynh, H. N., Ahern, A. T., Ball, K., Bates, K. H., Brock, C. A., Campos, T., Coggon, M. M., Crounse, J. D., de Gouw, J., DiGangi, J. P., Diskin, G. S., Gkatzelis, G. I., Halliday, H. S., Hu, L., Koss, A. R., Li, Y., Lyu, M., Michailoudi, G., Murphy, S. M., Nowak, J. B., Palm, B. B., Peischl, J., Permar, W., Perring, A. E., Pokhrel, R. P., Schafer, N. B., Schwarz, J. P., Sekimoto, K., Selimovic, V., Stockwell, C. E., Sullivan, A. P., Thornton, J. A., Wagner, N. L., Wang, S., Warneke, C., Wennberg, P. O., Zeng, L., Yokelson, R. J., Weber, R. J., and Xu, L.: Atmospheric Evolution of Brown Carbon from Wildfires in North America, Environ. Sci. Technol., 59, 17145–17159, https://doi.org/10.1021/acs.est.5c09020, 2025.

Duplissy, J., DeCarlo, P. F., Dommen, J., Alfarra, M. R., Metzger, A., Barmpadimos, I., Prevot, A. S. H., Weingartner, E., Tritscher, T., Gysel, M., Aiken, A. C., Jimenez, J. L., Canagaratna, M. R., Worsnop, D. R., Collins, D. R., Tomlinson, J., and Baltensperger, U.: Relating hygroscopicity and composition of organic aerosol particulate matter, Atmospheric Chemistry and Physics, 11, 1155–1165, https://doi.org/10.5194/acp-11-1155-2011, 2011.

Gkatzelis, G. I., Coggon, M. M., Stockwell, C. E., Hornbrook, R. S., Allen, H., Apel, E. C., Bela, M. M., Blake, D. R., Bourgeois, I., Brown, S. S., Campuzano-Jost, P., St. Clair, J. M., Crawford, J. H., Crounse, J. D., Day, D. A., DiGangi, J. P., Diskin, G. S., Fried, A., Gilman, J. B., Guo, H., Hair, J. W., Halliday, H. S., Hanisco, T. F., Hannun, R., Hills, A., Huey, L. G., Jimenez, J. L., Katich, J. M., Lamplugh, A., Lee, Y. R., Liao, J., Lindaas, J., McKeen, S. A., Mikoviny, T., Nault, B. A., Neuman, J. A., Nowak, J. B., Pagonis, D., Peischl, J., Perring, A. E., Piel, F., Rickly, P. S., Robinson, M. A., Rollins, A. W., Ryerson, T. B., Schueneman, M. K., Schwantes, R. H., Schwarz, J. P., Sekimoto, K., Selimovic, V., Shingler, T., Tanner, D. J., Tomsche, L., Vasquez, K. T., Veres, P. R., Washenfelder, R., Weibring, P., Wennberg, P. O., Wisthaler, A., Wolfe, G. M., Womack, C. C., Xu, L., Ball, K., Yokelson, R. J., and Warneke, C.: Parameterizations of US wildfire and

prescribed fire emission ratios and emission factors based on FIREX-AQ aircraft measurements, Atmospheric Chemistry and Physics, 24, 929–956, https://doi.org/10.5194/acp-24-929-2024, 2024.

Guo, H., Liu, J., Froyd, K. D., Roberts, J. M., Veres, P. R., Hayes, P. L., Jimenez, J. L., Nenes, A., and Weber, R. J.: Fine particle pH and gas–particle phase partitioning of inorganic species in Pasadena, California, during the 2010 CalNex campaign, Atmospheric Chemistry and Physics, 17, 5703–5719, https://doi.org/10.5194/acp-17-5703-2017, 2017.

Kannosto, J., Virtanen, A., Lemmetty, M., Makela, J. M., Keskinen, J., Junninen, H., Hussein, T., Aalto, P., and Kulmala, M.: Mode resolved density of atmospheric aerosol particles, Atmos. Chem. Phys., 2008.

Kupc, A., Williamson, C., Wagner, N. L., Richardson, M., and Brock, C. A.: Modification, calibration, and performance of the Ultra-High Sensitivity Aerosol Spectrometer for particle size distribution and volatility measurements during the Atmospheric Tomography Mission (ATom) airborne campaign, Atmospheric Measurement Techniques, 11, 369–383, https://doi.org/10.5194/amt-11-369-2018, 2018.

Kuwata, M., Zorn, S. R., and Martin, S. T.: Using Elemental Ratios to Predict the Density of Organic Material Composed of Carbon, Hydrogen, and Oxygen, Environ. Sci. Technol., 46, 787–794, https://doi.org/10.1021/es202525q, 2011.

Lee, T., Sullivan, A. P., Mack, L., Jimenez, J. L., Kreidenweis, S. M., Onasch, T. B., Worsnop, D. R., Malm, W., Wold, C. E., Hao, W. M., and Collett Jr., J. L.: Chemical Smoke Marker Emissions During Flaming and Smoldering Phases of Laboratory Open Burning of Wildland Fuels, Aerosol Science and Technology, 44, i–v, https://doi.org/10.1080/02786826.2010.499884, 2010.

Marple, V. A., Rubow, K. L., and Behm, S. M.: A Microorifice Uniform Deposit Impactor (MOUDI): Description, Calibration, and Use, Aerosol Science and Technology, 14, 434–446, https://doi.org/10.1080/02786829108959504, 1991.

McNaughton, C. S., Clarke, A. D., Howell, S. G., Pinkerton, M., Anderson, B., Thornhill, L., Hudgins, C., Winstead, E., Dibb, J. E., Scheuer, E., and Maring, H.: Results from the DC-8 Inlet Characterization Experiment (DICE): Airborne Versus Surface Sampling of Mineral Dust and Sea Salt Aerosols, Aerosol Science and Technology, 41, 136–159, https://doi.org/10.1080/02786820601118406, 2007.

Orsini, D. A., Ma, Y., Sullivan, A., Sierau, B., Baumann, K., and Weber, R. J.: Refinements to the particle-into-liquid sampler (PILS) for ground and airborne measurements of water soluble aerosol composition, Atmospheric Environment, 37, 1243–1259, https://doi.org/10.1016/S1352-2310(02)01015-4, 2003.

Rivera-Adorno, F. A., Azzarello, L., Robinson, M. A., Decker, Z. C. J., Washenfelder, R. A., Hayden, K., Franchin, A., Holmes, C. D., Young, C. J., Fredrickson, C. D., Palm, B., Schmidt, C.,

Soja, A., Gargulinski, E., Brown, S. S., Middlebrook, A. M., and Laskin, A.: Aircraft Measurements from a U.S. Western Wildfire Demonstrating Day and Night Differences in the Chemical Composition and Optical Properties of Biomass Burning Aerosols and Their Atmospheric Evolution, ACS Earth Space Chem., 9, 64–75, https://doi.org/10.1021/acsearthspacechem.4c00215, 2025.

Rollins, A. W., Rickly, P. S., Gao, R.-S., Ryerson, T. B., Brown, S. S., Peischl, J., and Bourgeois, I.: Single-photon laser-induced fluorescence detection of nitric oxide at sub-parts-per-trillion mixing ratios, Atmospheric Measurement Techniques, 13, 2425–2439, https://doi.org/10.5194/amt-13-2425-2020, 2020.

Schlosser, J. S., Braun, R. A., Bradley, T., Dadashazar, H., MacDonald, A. B., Aldhaif, A. A., Aghdam, M. A., Mardi, A. H., Xian, P., and Sorooshian, A.: Analysis of aerosol composition data for western United States wildfires between 2005 and 2015: Dust emissions, chloride depletion, and most enhanced aerosol constituents, Journal of Geophysical Research: Atmospheres, 122, 8951–8966, https://doi.org/10.1002/2017JD026547, 2017.

Schwarz, J. P., Gao, R. S., Fahey, D. W., Thomson, D. S., Watts, L. A., Wilson, J. C., Reeves, J. M., Darbeheshti, M., Baumgardner, D. G., Kok, G. L., Chung, S. H., Schulz, M., Hendricks, J., Lauer, A., Kärcher, B., Slowik, J. G., Rosenlof, K. H., Thompson, T. L., Langford, A. O., Loewenstein, M., and Aikin, K. C.: Single-particle measurements of midlatitude black carbon and light-scattering aerosols from the boundary layer to the lower stratosphere, Journal of Geophysical Research: Atmospheres, 111, https://doi.org/10.1029/2006JD007076, 2006.

Seinfeld, J. H., & Pandis, S. N.: Atmospheric chemistry and physics: From air pollution to climate change (3rd ed.). John Wiley & Sons., ISBN: 978-1-118-94740-1, 2016.

Sorooshian, A., Brechtel, F. J., Ma, Y., Weber, R. J., Corless, A., Flagan, R. C., and Seinfeld, J. H.: Modeling and Characterization of a Particle-into-Liquid Sampler (PILS), Aerosol Science and Technology, 40, 396–409, https://doi.org/10.1080/02786820600632282, 2006.

Sullivan, A. P., Guo, H., Schroder, J. C., Campuzano-Jost, P., Jimenez, J. L., Campos, T., Shah, V., Jaeglé, L., Lee, B. H., Lopez-Hilfiker, F. D., Thornton, J. A., Brown, S. S., and Weber, R. J.: Biomass Burning Markers and Residential Burning in the WINTER Aircraft Campaign, JGR Atmospheres, 124, 1846–1861, https://doi.org/10.1029/2017JD028153, 2019.

Sullivan, A. P., Pokhrel, R. P., Shen, Y., Murphy, S. M., Toohey, D. W., Campos, T., Lindaas, J., Fischer, E. V., and Collett Jr., J. L.: Examination of brown carbon absorption from wildfires in the western US during the WE-CAN study, Atmos. Chem. Phys., 22, 13389–13406, https://doi.org/10.5194/acp-22-13389-2022, 2022.